Dynamic large eddy simulation: Stability via realizability

Reza Mokhtarpoor and Stefan Heinz[a)]
Department of Mathematics, University of Wyoming, 1000 E. University Avenue, Laramie, Wyoming 82071, USA

The concept of dynamic large eddy simulation (LES) is highly attractive: such methods can dynamically adjust to changing flow conditions, which is known to be highly beneficial. For example, this avoids the use of empirical, case dependent approximations (like damping functions). Ideally, dynamic LES should be local in physical space (without involving artificial clipping parameters), and it should be stable for a wide range of simulation time steps, Reynolds numbers, and numerical schemes. These properties are not trivial, but dynamic LES suffers from such problems over decades. We address these questions by performing dynamic LES of periodic hill flow including separation at a high Reynolds number $Re = 37\,000$. For the case considered, the main result of our studies is that it is possible to design LES that has the desired properties. It requires physical consistency: a PDF-realizable and stress-realizable LES model, which requires the inclusion of the turbulent kinetic energy in the LES calculation. LES models that do not honor such physical consistency can become unstable. We do not find support for the previous assumption that long-term correlations of negative dynamic model parameters are responsible for instability. Instead, we concluded that instability is caused by the stable spatial organization of significant unphysical states, which are represented by wall-type gradient streaks of the standard deviation of the dynamic model parameter. The applicability of our realizability stabilization to other dynamic models (including the dynamic Smagorinsky model) is discussed. *Published by AIP Publishing.* https://doi.org/10.1063/1.4986890

I. INTRODUCTION

Large eddy simulation (LES)[1–8] can provide major contributions to analyses of engineering and environmental problems because of its ability to resolve turbulent motions at computational cost much below the cost of direct numerical simulation (DNS). A very attractive feature of LES is the possibility to calculate LES model parameters dynamically during the simulation.[9–11] Such dynamic LES has significant advantages compared to non-dynamic LES: they allow, e.g., to account for backscatter of energy and to apply appropriate LES model parameter variations in flow regions that are less turbulent or even laminar.[7,12–26]

In particular, one of the most relevant advantages of dynamic LES is the following. In many applications, it needs to account for walls, which imply a damping effect that has to be considered (its neglect leads to significant simulation performance deficiencies). This problem is known to be rather difficult, and there is no generally accepted solution.[27] This problem is even much more challenging if LES equations have to be combined with Reynolds-averaged Navier-Stokes (RANS) equations, which is often a requirement to efficiently deal with simulations of high Reynolds number flows.[28] A problem of such hybrid RANS-LES simulations is that modeled variables entering wall damping function models can become small in regions that are well resolved. An example for a modeled variable that can become small is the turbulence

Reynolds number, which scales the damping function in the turbulent viscosity model suggested by Bredberg *et al.*[29,30] The wall damping model, which is designed to consider relatively small values of modeled variables as being caused by the presence of a wall, can then predict wall damping in regions that are not affected by a wall. The use of dynamic LES appears to be the only reliable choice to deal with such problems.

However, a dynamic model parameter calculation can cause computational instabilities [as given for the original dynamic Smagorinsky model (DSM) used without stabilization[9]] due to the reasons that are currently not fully understood.[12] There are several empirical stabilization techniques in use, e.g., a clipping of dynamic LES parameters,[31] averaging over homogeneous directions,[9,32] or time averaging.[33] Such stabilization techniques are often difficult or even impossible to apply. With respect to many applications, there are no homogeneous directions in space. It is also difficult and time-consuming to find appropriate clipping values for dynamic LES parameters, which need to be chosen in dependence on the Reynolds number considered, the simulation time scale applied in simulations, and the numerical scheme. From a theoretical view point, standard empirical stabilizations of dynamic LES model parameters may be considered to be physically inconsistent. For example, averaging over cell faces corresponds to involving artificial correlations in an LES calculation.[26] Or, clipping of dynamic LES model parameters introduces a dependence of LES results on an arbitrary, artificial parameter (the clipping value).

Conceptually, it turned out that the application of the realizability principle is extremely useful for the design of

a)Author to whom correspondence should be addressed: heinz@uwyo.edu.

consistent dynamic LES models.[24] Realizability was proven to represent a valuable guiding principle for turbulence modeling,[5,34–37] and the use of realizable turbulence closure models was found to be relevant to many applications.[38–42] The basic way to make use of the realizability principle is to ensure that the subgrid-scale (SGS) stress, which represents the variance of a stochastic process, is derived from an existing stochastic process (a stochastic model for SGS velocities).[24,43–46] On this basis, the stochastic modeling approach also determines how the dynamic LES can be set up consistently. The latter approach results in a hierarchy of dynamic SGS models that can be used in non-equilibrium (with turbulent kinetic energy equation) or equilibrium versions (which apply an algebraic approximation to the turbulent kinetic energy). It is found that such dynamic models are similar to corresponding standard models like the DSM, but they are different:[25] see Sec. VII B. Application to turbulent channel flows,[25] the turbulent Ekman layer,[26] and periodic hill flows involving flow separation[28] demonstrates the excellent performance of these novel dynamic LES methods.

With respect to the stability of dynamic LES derived from an underlying stochastic SGS velocity model, it was found that the dynamic models considered were computationally stable (without any need for applying additional stabilization techniques) for turbulent channel[25] and turbulent Ekman layer[26] simulations, but only almost stable with respect to periodic hill flow simulations (the latter simulations were performed with a very soft clipping which was almost never applied).[28] The latter fact is not surprising because the numerical stability of dynamic LES represents a complex matter:[47,48] it can be expected that the use of physically consistent SGS stress models is one requirement for stable dynamic LES, but there are additional factors like the numerical scheme and simulation time step applied. With respect to using a physically consistent SGS stress model, it is of interest to note the following. The approach applied for the development of almost stable dynamic LES ensures realizability in the sense that the dynamic LES method is consistent with an underlying stochastic process, but this does not necessarily imply that the realizability of the SGS stress tensor as defined by Schumann[34] is ensured. In particular, similar to the observation made with respect to the numerical stability, it was found that the realizability of the SGS stress tensor is not always ensured. Thus, the question of what difference it makes to strictly enforce the SGS stress realizability was not addressed so far.

In extension of our previous work,[28] the latter question will be addressed here. First, we focus on the relationship between realizability and stability, i.e., we ask whether a dynamic LES model that is fully realizable (realizable not only by being based on an underlying stochastic process but also stress-realizable) is computationally always stable. The consideration of stress-realizability in the context of dynamic LES may be seen as a stabilization of dynamic LES. In this regard, it is relevant to see that the approach applied here is free of the shortcomings of usual stabilization methods described above: artificial information (correlations or clipping parameter values) is not involved. Second, to accomplish a deeper understanding of results, we address the question of what actually causes non-realizable models to being potentially

unstable. Third, we compare the stability and performance features of the fully realizable model obtained with corresponding features of other dynamic models which apply clippings or algebraic approximations to the subgrid kinetic energy. The term performance is used here to refer to the functionality of the dynamic parameter calculation (the simulation performance of the dynamic LES model considered was discussed in-depth in a recent publication).[28]

The paper is organized in the following way. In Secs. II and III, we present the modeling and simulation methods applied, respectively. The features of our new dynamic LES (which enforces stress-realizability), the relationship between realizability and stability, and reasons for the instability of dynamic LES are described in Secs. IV–VI. The transfer of our dynamic bound concept to other dynamic LES models and the performance of corresponding dynamic models are addressed in Sec. VII. Our conclusions obtained are summarized in Sec. VIII.

II. MODELING APPROACH

The equations considered will be introduced next. After presenting dynamic LES equations implied by a realizable stochastic velocity model, we present realizability bounds for dynamic model parameter variations, which follow from a realizable SGS stress constraint.

A. Realizable dynamic LES equations

The notion of realizability reflects the idea that an acceptable turbulence model must describe a velocity field that is physically achievable or realizable.[37] There are several ways to actually apply this constraint. One way is described in this section, and another way of working with the realizability constraint is described in Sec. II B.

By definition, the SGS stress is the variance of a stochastic process (the variance of SGS velocity fluctuations). In order to have a realizable dynamic SGS stress model, we may then require that the dynamic SGS stress is mathematically implied by an existing stochastic process that describes SGS velocity fluctuations in line with physics constraints. Accordingly, the most convenient way is to derive LES equations from an appropriate stochastic velocity model. This approach[24,30,43–46] implies the exact but unclosed filtered Navier-Stokes equations: the incompressible continuity and momentum equations are given by

$$\frac{\partial \widetilde{U}_i}{\partial x_i} = 0, \tag{1}$$

$$\frac{\widetilde{D}\widetilde{U}_i}{\widetilde{D}t} = -\frac{1}{\rho}\frac{\partial \widetilde{p}}{\partial x_i} + \frac{\partial (2\nu \widetilde{S}_{ij})}{\partial x_j} - \frac{\partial \tau_{ij}}{\partial x_j}. \tag{2}$$

Here, the tilde refers to space-averaged (LES) variables, and $\widetilde{D}/\widetilde{D}t = \partial/\partial t + \widetilde{U}_j \, \partial/\partial x_j$ is the filtered Lagrangian time derivative. In the above equations, $\widetilde{U}_i$ denotes components of the velocity vector, $\widetilde{p}$ is the pressure, ρ is the constant fluid density, ν is the constant kinematic viscosity, and $\widetilde{S}_{ij} = (\partial \widetilde{U}_i/\partial x_j + \partial \widetilde{U}_j/\partial x_i)/2$ is the rate-of-strain tensor. The SGS stress tensor τ_{ij} appears as an unknown on the right-hand

side (RHS) of the momentum equation. The sum convention is used throughout this paper. Although the equations are introduced here for incompressible flow, their extension to compressible flow is straightforward.[46]

The advantage of the underlying stochastic velocity model is that it implies in addition to the continuity equation (1) and conservation of momentum equation (2) also an equation for the SGS stress τ_{ij}. This equation reads

$$\frac{\widetilde{D}\tau_{ij}}{\widetilde{D}t} + \frac{\partial T_{kij}}{\partial x_k} = -\tau_{ik}\frac{\partial \widetilde{U}_j}{\partial x_k} - \tau_{jk}\frac{\partial \widetilde{U}_i}{\partial x_k} - \frac{2}{\tau_L}\left(\tau_{ij} - \frac{2}{3}c_0 k \delta_{ij}\right). \quad (3)$$

Here, T_{ijk} is the triple correlation tensor of velocity fluctuations, τ_L is the Lagrangian relaxation time scale of turbulent velocity fluctuations, and c_0 is a model constant that will be specified later (τ_L and c_0 are characteristic parameters of the underlying stochastic velocity model). For the following, it is helpful to rewrite Eq. (3) in terms of equations for the subgrid kinetic energy $k = \tau_{nn}/2$ and normalized anisotropy tensor $d_{ij} = (\tau_{ij} - 2k\delta_{ij}/3)/(2k)$. These equations are given by[46]

$$\frac{\widetilde{D}k}{\widetilde{D}t} + \frac{1}{2}\frac{\partial T_{knn}}{\partial x_k} + 2kd_{kn}\frac{\partial \widetilde{U}_n}{\partial x_k} = -\frac{2(1-c_0)k}{\tau_L}, \quad (4)$$

$$\frac{\widetilde{D}d_{ij}}{\widetilde{D}t} + \frac{1}{2k}\frac{\partial(T_{kij} - T_{knn}\delta_{ij}/3)}{\partial x_k} + \frac{d_{ij}}{k}\frac{\widetilde{D}k}{\widetilde{D}t} + d_{ik}\frac{\partial \widetilde{U}_j}{\partial x_k}$$
$$-\frac{2}{3}d_{kn}\frac{\partial \widetilde{U}_n}{\partial x_k}\delta_{ij} = -\frac{2}{\tau_L}d_{ij} - \frac{2}{3}\widetilde{S}_{ij}. \quad (5)$$

The latter equation can be used to derive a hierarchy of algebraic stress models.[46] The simplest model of this hierarchy is given by a linear stress model, which is obtained by assuming a balance of the RHS terms of Eq. (5), $d_{ij} = -\widetilde{S}_{ij}\tau_L/3$. This expression implies for the SGS stress τ_{ij} the model

$$\tau_{ij} = \frac{2}{3}k\delta_{ij} - 2\nu_t\widetilde{S}_{ij}, \quad (6)$$

where the subgrid viscosity is given by $\nu_t = k\tau_L/3$. By using the stress model equation (6), the velocity equation (2) reads now

$$\frac{\widetilde{D}\widetilde{U}_i}{\widetilde{D}t} = -\frac{\partial P}{\partial x_i} + 2\frac{\partial(\nu + \nu_t)\widetilde{S}_{ij}}{\partial x_j}, \quad (7)$$

where $P = (\widetilde{p}/\rho + 2k/3)$ is the modified pressure, and the k Eq. (4) reads

$$\frac{\widetilde{D}k}{\widetilde{D}t} = -\frac{1}{2}\frac{\partial T_{knn}}{\partial x_k} + 2\nu_t\widetilde{S}_{nk}\widetilde{S}_{nk} - \frac{2(1-c_0)k}{\tau_L}, \quad (8)$$

where the definition of $\widetilde{S}_{nk}$ is used. To close this equation, we use $T_{knn} = -2(\nu + \nu_t)\partial k/\partial x_k$ for triple correlations. The structure of this expression can be derived as a consequence of a transport equation for triple correlations, which is implied by the probability density function (PDF) transport equation considered.[44] By using $T_{knn} = -2(\nu + \nu_t)\partial k/\partial x_k$, the subgrid kinetic energy equation can be written as

$$\frac{\widetilde{D}k}{\widetilde{D}t} = \frac{\partial}{\partial x_j}\left[(\nu + \nu_t)\frac{\partial k}{\partial x_j}\right] + \nu_t|\widetilde{S}|^2 - \frac{2(1-c_0)k}{\tau_L}, \quad (9)$$

where $|\widetilde{S}| = (2\widetilde{S}_{ij}\widetilde{S}_{ji})^{1/2}$ refers to the characteristic strain rate. To be consistent with the usual LES dissipation rate [the negative last term on the RHS of Eq. (9)], we define the time scale τ_L by $\tau_L = 2(1-c_0)\Delta k^{-1/2}$. Hence, the subgrid kinetic energy equation reads

$$\frac{\widetilde{D}k}{\widetilde{D}t} = \frac{\partial}{\partial x_j}\left[(\nu + \nu_t)\frac{\partial k}{\partial x_j}\right] + \nu_t|\widetilde{S}|^2 - \frac{k^{3/2}}{\Delta}. \quad (10)$$

The closure of Eq. (10) still requires the definition of the SGS viscosity ν_t. The combination of $\nu_t = k\tau_L/3$ with $\tau_L = 2(1-c_0)\Delta k^{-1/2}$ implies the deterministic SGS model

$$\nu_t = C_s k^{1/2}\Delta, \quad (11)$$

where $C_s = 2(1-c_0)/3$. It is possible to simplify this model by using an algebraic expression for k (see Sec. VII B). However, we do not focus on this option because k is needed for the application of the dynamic bounds presented below. The use of a dynamic calculation of C_s offers many advantages: see the discussion in the Introduction. Such a dynamic LES method can be designed in complete consistency with the LES equations presented above by using an upscaled version of the underlying stochastic velocity model. The consequences of this approach can be illustrated in the following way. We consider the deviatoric component of the Leonard stress $L_{ij} = \overline{\widetilde{U}_i\widetilde{U}_j} - \overline{\widetilde{U}}_i\overline{\widetilde{U}}_j$ (equivalent to τ_{ij} on the test filter level), where the overbar refers to the test filter operation. The stochastic analysis approach provides $L_{ij}^d = -2C_s\Delta^T\sqrt{k^T}\overline{\widetilde{S}}_{ij}$ for the deviatoric component L_{ij}^d of the Leonard stress. This expression is the test filter level version of the deviatoric SGS stress $\tau_{ij}^d = -2C_s\Delta k^{1/2}\widetilde{S}_{ij}$ implied by Eq. (11). Here, we involve the test-filter subgrid kinetic energy $k^T = L_{nn}/2$ and filter width on the test-filter level $\Delta^T = 2\Delta$. By introducing the abbreviation $M_{ij} = 2\Delta^T\sqrt{k^T}\overline{\widetilde{S}}_{ij}$, the Leonard stress relation can also be written $L_{ij}^d = -C_sM_{ij}$. Here, both L_{ij}^d and M_{ij} are known such that $L_{ij}^d = -C_sM_{ij}$ can be used for the calculation of C_s. The setting

$$C_s = -\frac{L_{ij}^d M_{ji}}{M_{kl}M_{lk}} \quad (12)$$

can be shown to minimize the least squares error related to C_s settings. Formally, Eq. (12) is equivalent to multiplying $L_{ij}^d = -C_sM_{ij}$ with M_{ij}. The model equation (12) will be referred to as linear dynamic model combined with kinetic energy equation (LDMK). The corresponding k equation is given by Eq. (10).

The LDMK clearly differs from the DSM. First, the LDMK involves the subgrid kinetic energy k, which is approximated by an algebraic expression if the DSM is used. The LDMK can also be reduced to a model that involves an algebraic expression for k: see Sec. VII B. This expression [Eq. (33)] still differs from the DSM [Eq. (36)] because the equation used for dynamically calculating the dynamic parameter differs from the corresponding equation used in the DSM context.[25] The LDMK in its equilibrium mode (by using an algebraic expression for k) was applied very successfully as is (without using bounds) to turbulent channel[25] and turbulent Ekman layer[26] simulations. No significant difference was

found in comparison to using the model with k equation as described here.

B. Realizable SGS stress

In contrast to the consideration of realizability presented in Sec. II A, it is possible to relate realizability constraints to the property of the SGS stress tensor to be a positive semi-definite matrix.[36] With respect to the analysis presented here in Sec. II B, we would like to refer to two facts. First, in line with the consideration of incompressible flow in this paper, we will present this analysis for incompressible flow. However, the extension to compressible flow is simple: it just needs to replace $\widetilde{S}_{ij}$ by its deviatoric component $\widetilde{S}_{ij}^{d}$, and, correspondingly, $|\widetilde{S}|$ by $|\widetilde{S}^{d}|$. Second, the analysis presented here in Sec. II B does not make any other assumption than the structure of τ_{ij} given by Eq. (6) for the SGS stress. In particular, we do not assume any specific structure of the subgrid viscosity ν_t, this means our analysis results are applicable to all SGS stress models that use Eq. (6).

The SGS stress tensor τ_{ij} is a positive semi-definite matrix if it satisfies[34,36]

$$\tau_{ij} \geq 0 \quad for \quad i = j, \tag{13}$$

$$\tau_{ij}^2 \leq \tau_{ii}\tau_{jj} \quad for \quad i \neq j, \tag{14}$$

$$\det(\tau_{ij}) \geq 0. \tag{15}$$

We can use the first two conditions to obtain three realizability requirements for the SGS stress tensor,

$$\tau_{11} + \tau_{22} + \tau_{33} = 2k \geq 0, \tag{16}$$

$$\tau_{12}^2 + \tau_{13}^2 + \tau_{23}^2 \leq \tau_{11}\tau_{22} + \tau_{11}\tau_{33} + \tau_{22}\tau_{33}, \tag{17}$$

$$\det(\tau_{ij}) \geq 0. \tag{18}$$

The SGS stress tensor is assumed to have an eddy viscosity structure given by Eq. (6). Correspondingly, the three realizability conditions Eqs. (16)–(18) can be written as

$$k \geq 0, \tag{19}$$

$$\left(\frac{\nu_t|\widetilde{S}|}{k}\right)^2 \leq \frac{4}{3}, \tag{20}$$

$$\left(\frac{\nu_t|\widetilde{S}|}{k}\right)^2 \left\{1 + 12\frac{\nu_t|\widetilde{S}|}{k}\frac{\det(\widetilde{S}_{ij})}{|\widetilde{S}|^3}\right\} \leq \frac{4}{9}. \tag{21}$$

To simplify the presentation, we introduce two nondimensional variables related to the SGS viscosity ν_t and $\det(\widetilde{S}_{ij}^{d})/|\widetilde{S}|^3$,

$$\nu_t^* = \frac{\sqrt{3}}{2}\frac{\nu_t|\widetilde{S}|}{k}, \qquad s = \frac{3^{1.5}\det(\widetilde{S}_{ij})}{(\widetilde{S}_{mn}\widetilde{S}_{mn})^{1.5}}. \tag{22}$$

Therefore, the three realizability conditions finally read

$$k \geq 0, \tag{23}$$

$$|\nu_t^*| \leq 1, \tag{24}$$

$$\nu_t^{*2}\left\{1 + \frac{2\sqrt{2}}{3}s\nu_t^*\right\} \leq \frac{1}{3}. \tag{25}$$
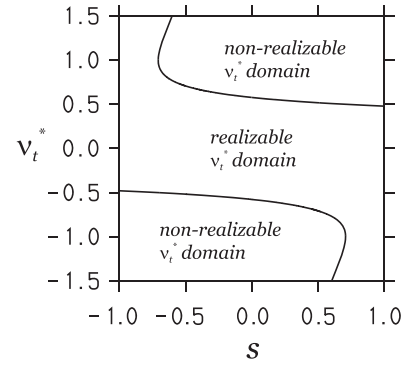
FIG. 1. Solutions to $\nu_t^{*2}(1 + 2\sqrt{2}s\nu_t^*/3) = 1/3$, see Eq. (25).

A relevant property of s follows from linear algebra. For any $n \times n$ matrix A, Hadamard's inequality implies

$$|\det(A_{ij})| \leq n^{-n/2}\|A\|^n, \tag{26}$$

where $\|A\| = (A_{ij}A_{ji})^{1/2}$ refers to the Hilbert Schmidt norm of A. The equality sign in this relation applies to the case of equal diagonal entries and zero non-diagonal entries. Using this theorem, we conclude that $|s| \leq 1$.

The realizable domain for ν_t^*, this means the values of ν_t^* that satisfy the inequality equation (25), is shown in Fig. 1. The use of a realizability criterion that is independent of s significantly simplifies the use of this criterion. This can be accomplished by the constraint that ν_t^* varies between the allowed values at $s = -1$ and $s = 1$, this means $|\nu_t^*| \leq 0.479\,17 = 23/48$. To summarize, given that $k \geq 0$, the condition to ensure that the SGS stress tensor τ_{ij} is a positive semi-definite matrix is to ensure that $|\nu_t^*| \leq 23/48$, which satisfies both Eqs. (24) and (25).

According to the realizability condition $|\nu_t^*| \leq 23/48$ and $\nu_t = C_s k^{1/2}\Delta$ derived above, we find the following C_s realizability condition for the LDMK,

$$|C_s| \leq \frac{23}{24\sqrt{3}}\frac{k^{1/2}}{\Delta|\widetilde{S}|}. \tag{27}$$

To differentiate between the realizability concepts presented in Secs. II A and II B, we will refer below to the realizability concept leading to Eq. (27) as stress-realizability, whereas the realizability concept described in Sec. II A will be referred to as PDF-realizability. If there is no further indication, the notation LDMK used below refers to the LDMK combined with the use of the realizability bounds, Eq. (27).

III. PERIODIC HILL FLOW SIMULATIONS

Next, we introduce the flow considered in simulations, the discretization of equations, and the simulation setup. It is worth noting that the same flow was considered in our recent analysis of hybrid dynamic LES methods,[28] where stress-realizability was not addressed.

A. Periodic hill flows

We consider separated flow over two-dimensional hills as illustrated in Fig. 2. This flow configuration creates a variety
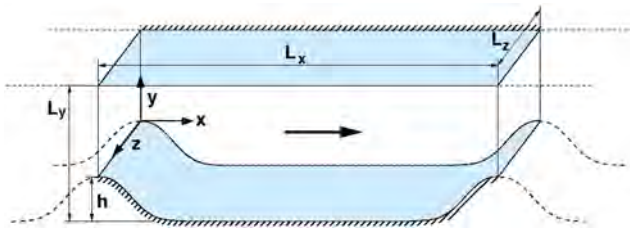
FIG. 2. The geometry of two-dimensional periodic hill flows.[54]
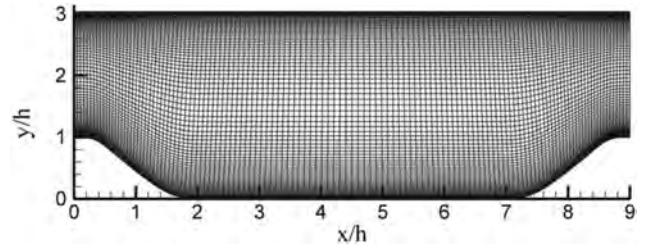
FIG. 3. Computational domain of two-dimensional hill flow simulations: the reference curvilinear grid is shown.

of relevant flow features such as separation, recirculation, and natural reattachment. The configuration follows the numerical work of Mellen *et al.*[49] who adjusted Almeida *et al.*'s[50] experimental geometry to meet numerical needs. Periodicity was assumed in streamwise directions and statistical homogeneity was assumed in spanwise directions to facilitate numerical studies with lower computational cost and to apply simple periodic boundary conditions in streamwise and spanwise directions. After Mellen *et al.*,[49] this geometry has been used for various numerical studies and served as a benchmark to test models. Experimental results were presented by Rapp and Manhart.[51–54] Temmerman and Leschziner,[55,56] Jakirlic *et al.*,[57,58] Jang *et al.*,[59] Fröhlich *et al.*,[60] Breuer *et al.*,[61] and Balakumar *et al.*[62] used this configuration to test turbulence models and numerical methods.

Numerical simulations of this flow at $Re = 37\,000$ have been performed by Chaouat and Schiestel.[63] They applied their PITM hybrid model[64] on grids ranging from 240×10^3 to 960×10^3 points. PITM simulation results were compared with RANS Reynolds stress model (RSM) results. The authors observed that in contrast to the PITM simulations, the RSM computations showed important weaknesses regarding the prediction of this flow caused by the lack of large unsteady eddies.

Recently, a numerical study of this flow at $Re = 37\,000$ has been published by us.[28] The dynamic LES model (using a clipping which was almost never applied) was compared with dynamic RANS-LES and RANS. Different grid resolutions ranging from 60×10^3 to 20×10^6 cells were used, and also different Reynolds numbers were considered. It was found that the dynamic RANS-LES performs better than RANS and pure LES that is not fully resolved.

B. Discretization of equations

All dynamic SGS models that are discussed in this study have been implemented in the OpenFOAM CFD Toolbox.[65] The calculations have been performed using a finite-volume based method with the numerical grid being used as the LES filter. The convection term was discretized using a second-order central difference scheme in the momentum equation and a bounded second-order central difference (BCD) scheme [which is implemented based on a normalized variable diagram (NVD) limiter[66]] is used in the turbulence transport equations to ensure a stable solution. All other terms were discretized using a second-order central difference scheme. The pressure gradient that drives the flow in the channel has been adjusted dynamically to maintain a constant mass flow rate. PISO algorithm was used for the pressure-velocity coupling.[67]

The resulting algebraic equations for all the flow variables except the pressure have been solved iteratively using a preconditioned bi-conjugate gradient method with a diagonally incomplete LU preconditioning at each time step. The Poisson equation for pressure was solved using an algebraic multi-grid solver. Time marching was performed using a second-order backward difference scheme.

C. Simulation setup

Figure 3 shows the computational domain applied in our simulations. The size of the computational domain is $L_x = 9h$, $L_y = 3.035h$, and $L_z = 4.5h$ in streamwise (x), wall normal (y), and spanwise (z) directions, respectively, where h is the height of the hill. The hill crest is located at $(x,y)/h = (0,1)$. The Reynolds number $Re = U_b h/\nu$ is $Re = 37\,000$ based on the hill height and bulk velocity above the hill crest at $x = 0$. At the bottom and top, the channel is constrained by solid walls. No-slip and impermeability boundary conditions are used at these walls. Periodic boundary conditions are employed in streamwise and spanwise directions. Throughout of the paper, h and U_b are used as reference quantities for a length and velocity. All data presented are made dimensionless with these quantities.

In a recently published paper,[28] we investigated the same flow using pure LES and hybrid RANS-LES models. We also studied grid effects for both methods for grids ranging from 60K to 20M cells. Here, our aim is to analyze the stability of dynamic models. Therefore, we will use a reference grid for all our results presented here. From our previous studies, we found that the grid of $N_x \times N_y \times N_z = 128 \times 80 \times 48$ with 500K cells is a well appropriate mesh for the present study.

Our computations are initialized by a uniform bulk velocity U_b (except for correlation functions: for them we restarted our calculations with stationary solutions). After 20 flow-through times (FTT), mean quantities were obtained by averaging over 140 FTT and averaging in the spanwise direction. Usually (see the Δt variations below), the time step Δt (all Δt are given in seconds) was chosen to imply a maximum CFL number of 0.5 and an averaged CFL number of about 0.1 (for stability analysis, we used CFL numbers ranging between 0.1 and 0.8).

IV. REALIZABILITY AND STABILITY

The numerical stability of dynamic LES can be expected to depend on a variety of factors: for example, the physical consistency of the SGS stress model, the numerical scheme,

and the simulation time step applied.[47,48] In particular, the physical consistency of the SGS stress model (which is reflected by realizability constraints) can be expected to have a major impact on the stability of simulations: it appears to be plausible that a flow that cannot be realized in reality also cannot be realized numerically. However, there are questions related to this general notion. (i) For example, is stress-realizability indeed related to stability? (ii) Is stress-realizability a required or a sufficient condition for stability? (iii) What actually causes instability, and why is it related to realizability? These questions will be addressed in the following as an extension of our recent analysis of the performance of the LDMK (combined with a very soft clipping which was almost never applied).[28] An detailed analysis of mean velocities, Reynolds stresses, and other flow features for several grids can be found elsewhere,[28] this means we focus here immediately on features relevant to the stability issue.

It is a broadly accepted view that the stability of dynamic LES is, basically, related to the setup of the dynamic LES model parameter calculation. Our previous results clearly show the advantage of using a PDF-realizable model.[24,25] In particular, we found that our dynamic model was computationally stable (without any need for applying additional stabilization techniques) for turbulent channel[25] and turbulent Ekman layer[26] simulations. However, with respect to periodic hill flow simulations,[28] it turned out that these simulations were almost always but not always stable.

The latter fact is illustrated in Fig. 4, which shows the time history of C_s calculated by the LDMK and the upper and lower realizability bounds for two probe points for 30 FTT. The locations of probe points P1 and P2 are shown in Fig. 5(a). The red and blue circles in Fig. 4 indicate the times at which C_s values hit the upper and lower realizability bounds, respectively. At P1, we found that over 30 FTT (corresponding to 150 000 iterations) on average 2% of C_s values hit the upper (positive) realizability bound, and about the same number of C_s values hits the lower (negative) realizability bound. With respect to the probe point P2,

we observed corresponding hittings in about 0.4% of cases (again, the lower and upper bounds had about the same hitting rates).

To assess the realizability of the model in the entire flow field, we defined a local (at each cell) hitting probability (HP) by the expressions

$$\text{HP}^+ = \frac{N^+}{N}, \qquad \text{HP}^- = \frac{N^-}{N}. \qquad (28)$$

Here, N^+ and N^- refer to the numbers of positive and negative bound hittings, respectively, and N refers to the total number of iterations. Figure 5 [left-hand side, (LHS)] shows the contour plots of HP^+ and HP^- for $\Delta t = 0.002$. Here and in the following, contour plots show the spatial distribution of averaged variables given in profile plots. It can be seen that HP^+ and HP^- are smaller than 0.005 in 95% of the flow field. Only in the shear layer immediately after the top of the leeward hill, these probabilities increase up to 0.02. First, this shows that the original LDMK model, which is only PDF-realizable, i.e., it is not combined with the realizability bounds, Eq. (27), is almost always realizable, but it is not always realizable, which may promote instability. Second, these results do also indicate that the stress-realizable LDMK [the LDMK combined with the use of the realizability bounds Eq. (27)] is stable. We call a model stable when it does not become unstable for 100 FTT.

The relative low number of LDMK bound hittings reported here (the view that the LDMK is almost always realizable) could be implied by relatively weak variations of C_s. This view can be addressed in terms of Fig. 15 (see Sec. VII D) which shows instantaneous variations of ν_t/ν as a measure for the significance of C_s variations. This figure shows strong variations of the subgrid viscosity ratio ν_t/ν in between ± 10, i.e., the variations of C_s are not small.

In extension of the findings reported above, let us consider the effect of the simulation time step Δt on the realizability of the model. Figure 5 compares LDMK hitting probabilities for two time steps Δt. We see that an increasing simulation time step increases the fluctuations of C_s values such that the bound

(a)

(b)
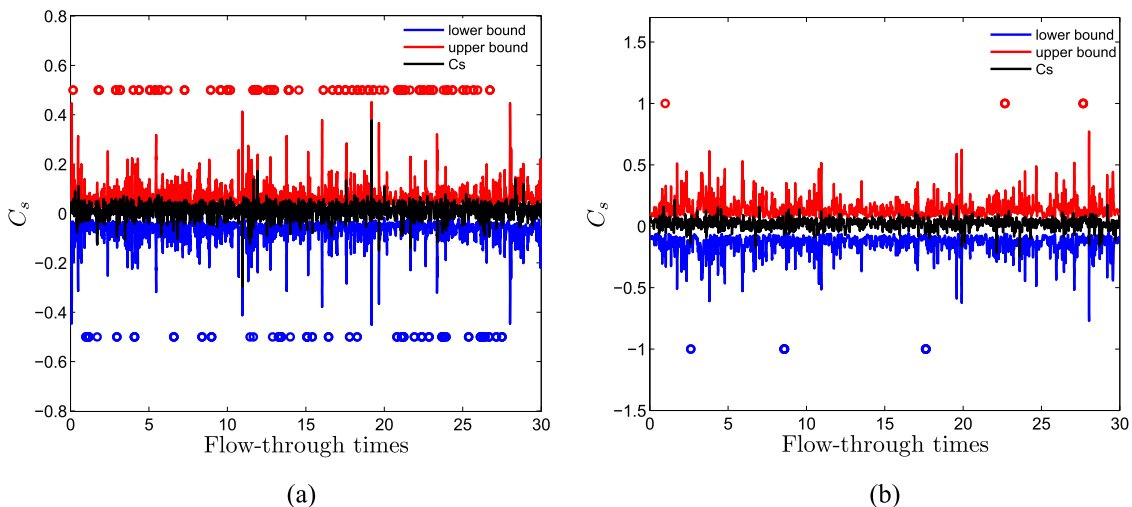
FIG. 4. LDMK time histories of C_s and its realizability bounds for the last 30 FTT at two probe points P1 and P2 [see Fig. 5(a)]. The red and blue circles indicate times at which C_s values hit the upper and lower realizability bounds, respectively. The time step is $\Delta t = 0.002$.
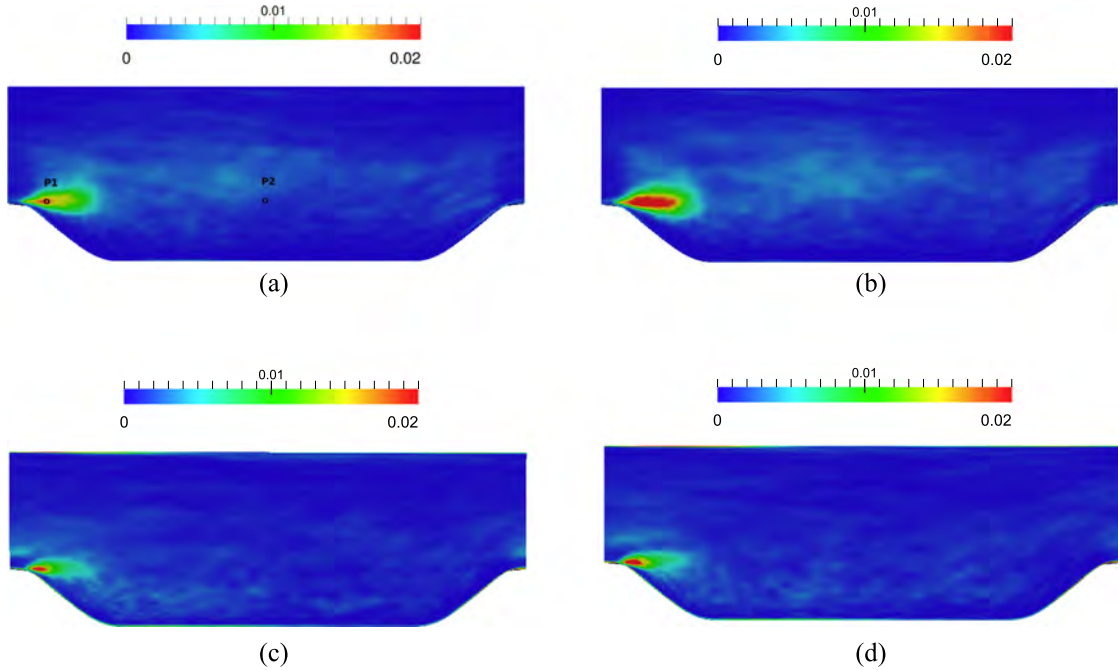
FIG. 5. LDMK positive (HP$^+$) and negative (HP$^-$) bound hitting probabilities for $\Delta t = 0.002$ (left) and $\Delta t = 0.008$ (right). (a) HP$^+$ for $\Delta t = 0.002$, (b) HP$^+$ for $\Delta t = 0.008$, (c) HP$^-$ for $\Delta t = 0.002$, and (d) HP$^-$ for $\Delta t = 0.008$.

hitting probabilities increase as well. A possible explanation for the fact that C_s fluctuations are increased by an increased Δt is the following. C_s is calculated by the constraint to minimize the quadratic error of $L_{ij}^d = -C_s M_{ij}$. Compared to a relatively large Δt, the fluctuations of C_s will be smaller if there is more often the opportunity to respond to changing flow conditions (to minimize the imbalance of $L_{ij}^d = -C_s M_{ij}$ caused by any C_s settings).

The use of stress bounds ensures stability, but it could be that the stress bounds are more restrictive than needed for stability. Or, in other words, can a model that is slightly unrealizable still be stable? To address this question, we used LDMK versions which apply bounds that are (1.2, 1.5, 2) times larger than the regular bounds given by Eq. (27). We refer to these models as LDMK-1.2B, LDMK-1.5B, LDMK-2B, respectively. Table I summarizes the stability analysis results for the LDMK and its extended bound versions. We see that the LDMK is strongly stable for a wide range of time steps $10^{-3} \leq \Delta t \leq 10^{-2}$, which correspond to CFL numbers ranging between 0.1 and 0.8. On the other hand, LDMK-1.2B is only stable for time steps $\Delta t = 0.001$ and 0.002, and LDMK-1.5B and LDMK-2B are even unstable for the smallest Δt considered here.

The findings reported in this Sec. IV can be summarized in the following way. First, the original LDMK model, which is only PDF-realizable, produces significant subgrid viscosity variations. It is almost always realizable, but it is not always realizable. There are a relatively low number of cases where C_s is outside of bounds, but these rare events can cause instability. Second, an increased simulation time step increases C_s fluctuations and, therefore, the instability risk. Third, the LDMK is stable for wide variations of the simulation time step. A model that is not stress-realizable can become unstable. Therefore, our results indicate that realizability (PDF-realizability and stress-realizability) is a required and sufficient condition for stability.

It is obvious that a better understanding of the mechanism of how computational instabilities are generated would be highly beneficial. So far there is no generally accepted explanation of how such instabilities occur, which turned out to be a very difficult question.[12,47,48] We will address this question in Secs. V and VI in order to accomplish a more comprehensive understanding of our results presented above. There is, in particular, the question what can cause a model that is not fully realizable to become computationally unstable.

V. INSTABILITY ANALYSIS I: TIME AND SPACE CORRELATIONS

According to our knowledge, the only hypothesis of the instability mechanism of dynamic LES presented so far is Lund *et al.*'s conclusion that a large temporal C_s auto-correlation, which causes negative eddy viscosity to persist for a long time, can cause a divergence of the total energy.[12] Let us reconsider this view by asking whether significant correlations of negative C_s values in space or time can be a reason for instabilities.

TABLE I. Stability of the LDMK and its extended bound versions for various time steps Δt.

Simulation	$\Delta t = 0.001$	$\Delta t = 0.002$	$\Delta t = 0.004$	$\Delta t = 0.008$	$\Delta t = 0.01$
LDMK	Stable	Stable	Stable	Stable	Stable
LDMK-1.2B	Stable	Stable	Unstable	Unstable	Unstable
LDMK-1.5B	Unstable	Unstable	Unstable	Unstable	Unstable
LDMK-2B	Unstable	Unstable	Unstable	Unstable	Unstable
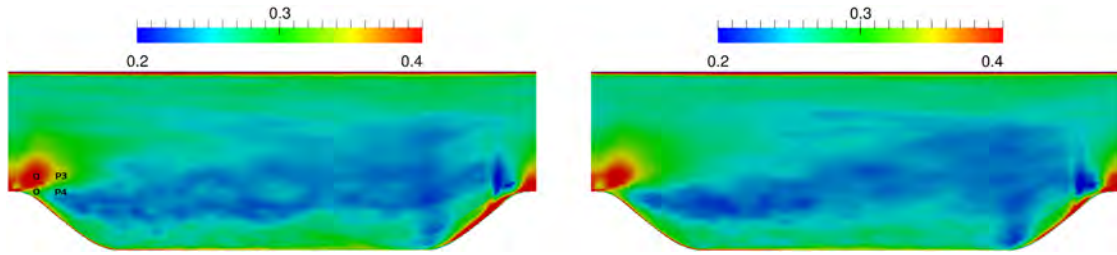
FIG. 6. Contour plots of the probability of negative C_s values (PNCs) for the stable LDMK (left) and unstable LDMK-2B (right). The time step is $\Delta t = 0.002$.

A. Approach applied

Regarding this question, we need a model that becomes unstable, but we also need a sufficient number of samples for the correlation function calculation. Thus, we use the unstable LDMK-2B model (with $\Delta t = 0.002$), which becomes unstable after 56 FTT. The LDMK-2B simulation was initialized by using a converged solution obtained from the LDMK.

We need to decide about the points at which correlation functions are calculated. A reasonable view is to calculate correlation functions in a region where the occurrence of negative C_s is high. To quantify the relative amount of negative C_s values, we consider at each cell the probability of the occurrence of negative C_s (PNCs), which is defined by PNCs = N_{neg}/N. Here, N_{neg} refers to the number of iterations in which C_s is negative, and N is again the total number of iterations. Figure 6 shows the contours of PNCs obtained from the LDMK and LDMK-2B. In particular, red shows the region where PNCs ≥ 0.4. It is worth noting that there is no significant time step effect on the PNCs distribution (not shown here). It can be seen that there is actually no
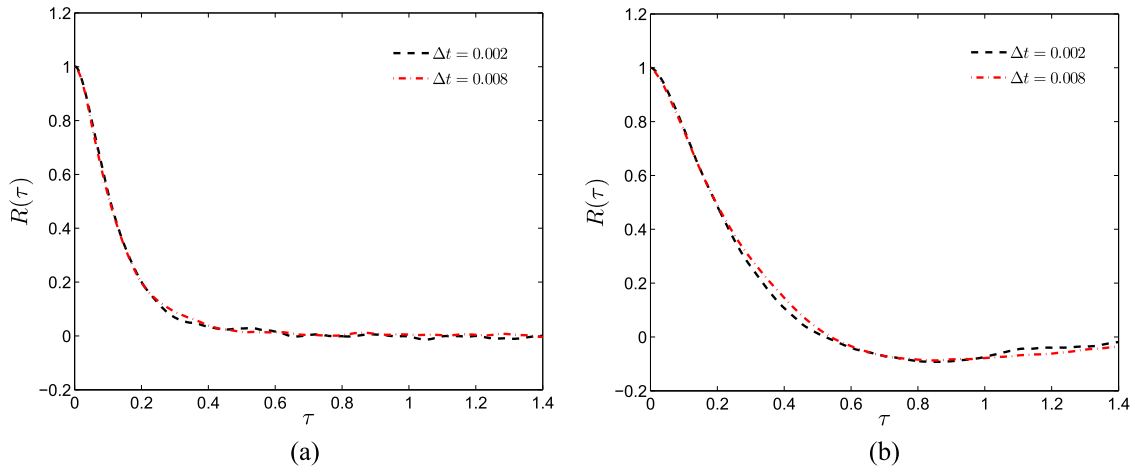
FIG. 7. LDMK temporal correlation functions: the effect of the simulation time step at P3 and P4. (a) P3 and (b) P4.
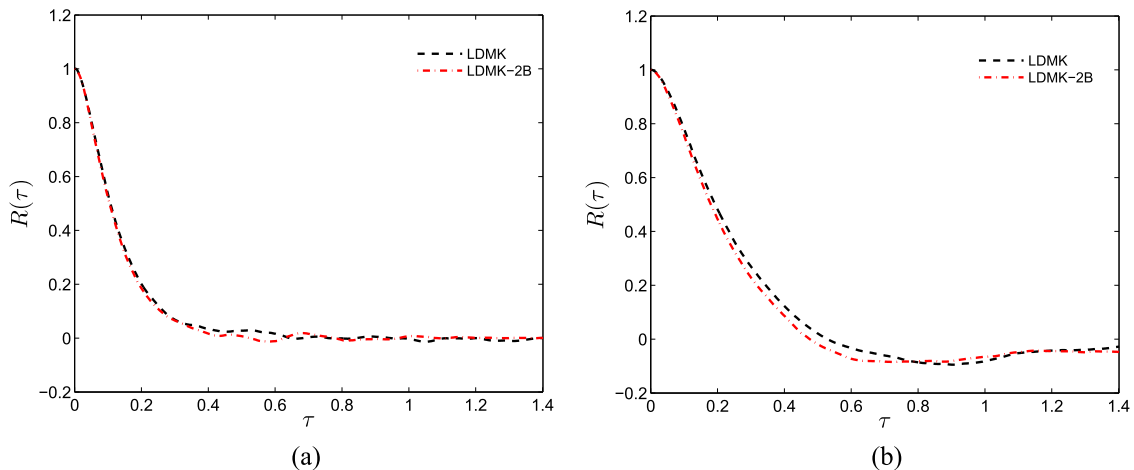
FIG. 8. LDMK and LDMK-2B temporal correlation functions at P3 and P4. The time step is $\Delta t = 0.002$. (a) P3 and (b) P4.

difference between the PNCs distributions of the stable LDMK and unstable LDMK-2B. The time correlation functions presented below are calculated at two points: at P3, which is located in the center of the bubble where we have the highest occurrence of negative C_s values [see Fig. 6(a)] and at another point P4, which is located in the shear layer where we have large gradients of flow field quantities.

B. Correlations in time

The temporal auto-correlation function $R(\tau)$ of C_s at a specific time t_0 is calculated by

$$R(\tau) = \frac{\langle C'_s(t_0) C'_s(t_0 + \tau) \rangle}{\langle C'_s(t_0) C'_s(t_0) \rangle}. \qquad (29)$$
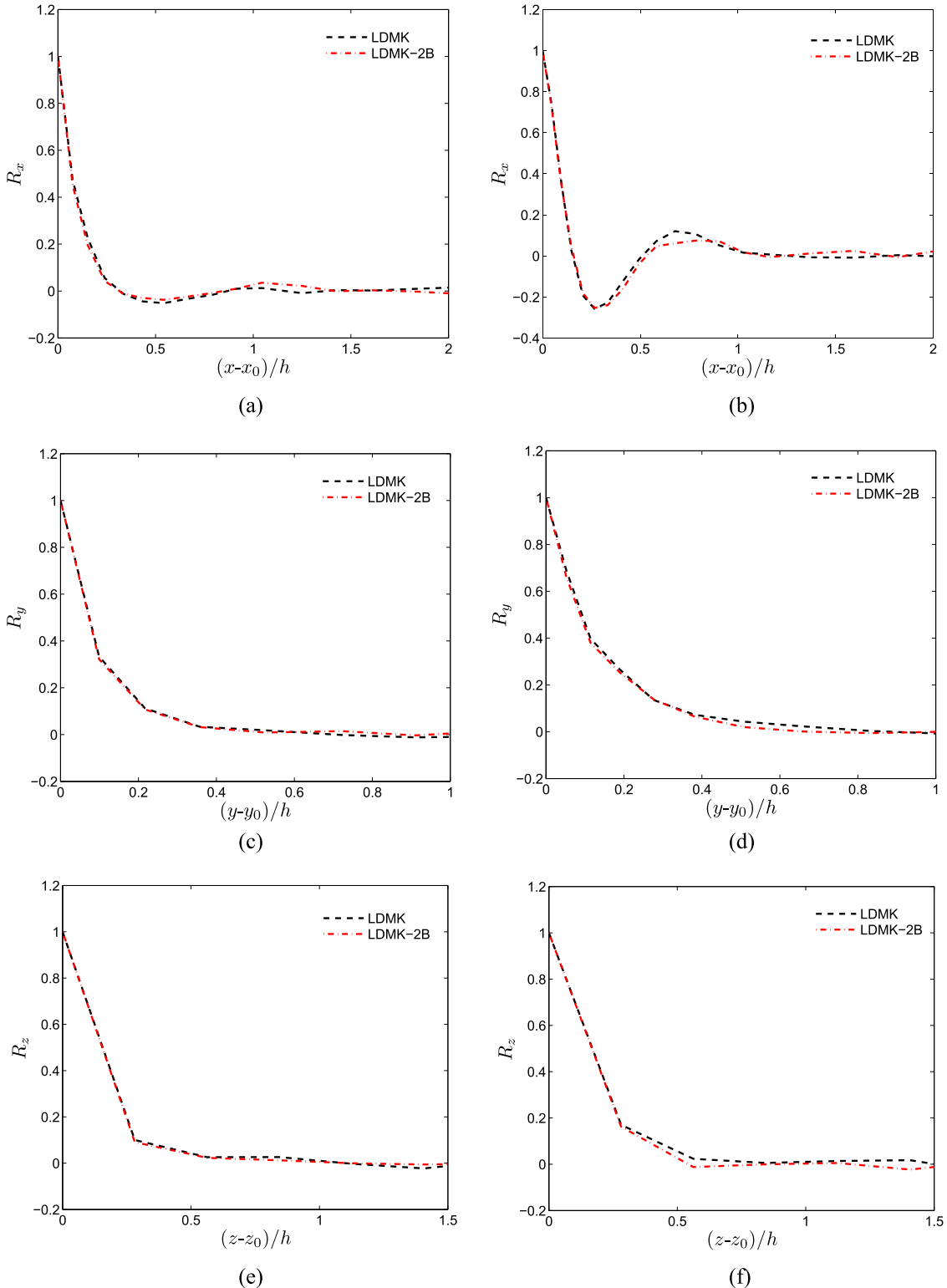
FIG. 9. LDMK and LDMK-2B space correlation functions at P3 and P4. The time step is $\Delta t = 0.002$. [(a), (c), and (e)] P3 and [(b), (d), and (f)] P4.

Here $C_s' = C_s - \langle C_s \rangle$ is the fluctuation of C_s at a specific time ($\langle C_s \rangle$ is the ensemble-averaged mean of C_s). Temporal correlation functions were calculated for the stable LDMK and unstable LDMK-2B. The LDMK-2B model becomes unstable after 56 FTT, which corresponds to 560 s. Independent samples were taken successively every 1.4 s because the characteristic correlation times at P3 and P4 are 0.6 s and 1.4 s, respectively (see Fig. 7). At one point, we obtain in this way a relatively low number 560/1.4 = 400 samples. The number of samples was increased by using 40 samples in the homogeneous z direction: at P3 and P4, we considered samples having the same x and y but different z coordinates. This increased the total number of samples used in the time correlation calculations to 400 × 40 = 16 000 samples. With respect to the LDMK, we could have used many more samples, but we preferred to use the same amount of samples for the correlation functions of both models.

First, we consider the simulation time step effect on correlation functions. Figure 7 shows the LDMK temporal correlation function using two time steps $\Delta t = (0.002, 0.008)$. It can be seen that these correlation functions are actually unaffected by different time steps. Next, let us compare the temporal correlation functions of stable and unstable models. Figure 8 compares the LDMK and LDMK-2B correlation functions at P3 and P4. It can be seen that there is, basically, no difference between the LDMK and LDMK-2B correlation functions.

The results reported here seem to lead to the conclusion that there is a difference to the conclusions presented by Lund *et al.*[12] However, a closer look shows that this is not the case. Lund *et al.* considered simulations of homogeneous isotropic turbulence using a pseudo-dynamic model where the model coefficient was taken from a Gaussian distribution of random numbers with specified mean, standard deviation, and correlation time. First, the flow considered is very different from our flow. Second, the correlation time considered is not equivalent to the characteristic temporal correlation of C_s: Lund *et al.*'s[12] correlation time is a technical (non-physical) parameter given by $(1 - \eta)\Delta t$, where η is the fraction of C_s values that are randomly regenerated at each time step Δt. Third, Lund *et al.*'s[12] dynamic coefficient calculation is not part of the simulation, it represents an external input to the simulations. Due to these facts, the conclusions obtained by us and Lund *et al.*[12] are very different: we considered the physical temporal correlation of C_s, whereas Lund *et al.*[12] considered the response of simulations to external disturbances scaled in terms of $(1 - \eta)\Delta t$ and the standard deviation of artificial C_s values imposed by their algorithm.

C. Correlations in space

In addition to considering the temporal correlation of C_s values, we also studied three-dimensional C_s correlations in space (which were not considered by Lund *et al.*[12]), to see whether there is a significant difference to the results obtained for the temporal correlations.

The spatial auto-correlation R_x of C_s in the x direction is calculated by

$$R_x = \frac{\langle C_s'(x_0) C_s'(x) \rangle}{\langle C_s'(x_0) C_s'(x_0) \rangle}. \tag{30}$$

Here, x_0 is the x-coordinate of the point where the correlation function is calculated. Spatial correlations in the y and z directions are calculated correspondingly. Independent samples were taken in time and in homogeneous directions. Regarding R_x and R_y, we used an averaging time $L_x/(3U_b) = 3$ s, corresponding approximately to the time needed for the fluid to pass one third of the computational domain. The LDMK-2B is stable for 560 s, so we generated only about 560/3 = 186.7 samples in this way. The sample number was increased by sampling in the homogeneous z-direction. The total sample number obtained was then 186.7 × 40 ≈ 7500. Regarding R_z, there is no homogeneous direction that is useful to increase the sample number. For the stable LDMK model, we collected 6000 samples in time by using the averaging time window mentioned above. An analysis showed that it is well possible to decrease the averaging time window for calculating R_z down to 0.5 s. Hence, we were able to calculate R_z for the LDMK-2B by using 560/0.5 = 1120 samples.

Figure 9 compares the LDMK and LDMK-2B spatial correlation functions of C_s at P3 and P4. It can be seen that there are no significant differences between stable and unstable dynamic models. The structure of correlation functions reflects the well-known features of correlation functions in wall bounded flows.[25,26]

First, it turns out, therefore, that the results reported about the C_s correlations in space are fully consistent with the results obtained for C_s correlations in time. Second, we can exclude C_s correlations as being the main reason for computational instabilities.

VI. INSTABILITY ANALYSIS II: TIME AND SPACE IMBALANCES

After excluding C_s correlation functions as a reason for the generation of computational instabilities in Sec. V, let us continue our analysis of instability reasons by considering other plausible possibilities.

A. Approach applied

The next obvious possibility to explain instability reasons is to consider significant imbalances in time or space. In this case, we are interested in clearly seeing the difference between stable and unstable LES models, which means we are interested in very unstable LES models. For addressing this question, we will consider the LDMK without the realizability bounds Eq. (27) but combined with a constant clipping instead of the bounds. We will use the notation LDMK-CC to refer to this LDMK combined with a constant clipping, and we will use LDMK-CC-xx, where xx refers to the negative clipping applied.

The unstable model considered for comparisons is the LDMK-CC-0.2, which refers to the LDMK combined with a negative clipping $C_{clip} = -0.2$. This model is very unstable, instability occurs in less than 5 FTT. The use of $C_{clip} = -0.2$ in conjunction with considering a very unstable model may be surprising regarding our recent analysis of hybrid RANS-LES and dynamic LES for the same flow.[28] The latter results led to the conclusion that the dynamic hybrid RANS-LES model was stable even for larger negative values, we used this

model combined with $C_{clip} = -0.5$. This can be explained by the fact that in our dynamic hybrid RANS-LES model, most cells in the wall region (up to 20 cells above the wall) are in the RANS layer such that the dynamics LES model parameter calculation was only used above this layer. Then, pure dynamic LES simulations were initialized by using converged dynamic hybrid RANS-LES results. This approach resulted in the conclusion that $C_{clip} = -0.5$ was sufficient to ensure stability. On the other hand, LDMK-CC simulations were initialized here with the bulk velocity, which is the usual way to initialize flow simulations in the absence of converged results obtained by other appropriate models. For ensuring stability in this case, we concluded that $C_{clip} = -0.05$ was needed. Due to reasons explained below, we consider two stable models (the LDMK-CC-0.02 and LDMK-CC-0.05) for comparisons with the unstable LDMK-CC-0.2.

What can be the reason for instabilities? One obvious possibility is given by the frequent occurrence of unphysical states, which can be measured in terms of the probability of dynamic bound hittings. To address this possibility, we compared the unstable LDMK-CC-0.2 with the stable LDMK-CC-0.05, where $\Delta t = 0.002$. As expected, the LDMK-CC-0.2 hitting probabilities are much higher than the LDMK-CC-0.05 hitting probabilities. However, the LDMK-CC-0.2 hitting probabilities are similar but below the hitting probabilities obtained from the dynamically bounded LDMK for $\Delta t = 0.08$, which is stable [see Figs. 5(b) and 5(d)]. Therefore, it appears to be very unlikely that the frequent occurrence of unphysical states causes instability.

Another potential reason for the generation of instabilities can be given by large (negative) C_s fluctuations. The notion of large fluctuations can have several meanings. A first approach to this question is to look at the appearance of negative values of the total viscosity (which is the sum of the molecular and subgrid viscosity) in the diffusion terms of the momentum or subgrid kinetic energy equations. Due to reasons described in Sec. VII A, the enforcement of positive total viscosity values is sufficient for the stabilization of dynamic LES models. However, the latter does not mean that negative total viscosity values cause instability. Figure 10 shows snapshots of the total viscosity ratio $(\nu_t + \nu)/\nu$ for the stable LDMK and a very unstable LDMKCC-02 model (see Sec. VI B) at the time of divergence. It can be seen that the stable model implies a significant amount of negative total viscosity in about 10% of cells. We can also see that there is no significant difference between the stable and very unstable models regarding the amount of negative total viscosity. Thus, the observations made here do not support the view that negative values of the total viscosity are the basic reason for instability.

A second approach to address the relevance of large C_s fluctuations is to look at C_s standard deviations. This possibility is considered in detail in Secs. VI B and VI C.

B. C_s standard deviation: Imbalances in time

First, we consider C_s standard deviations in time to study the influence of large C_s fluctuations on stability. This standard deviation can be calculated in several ways. Here, we are interested in a flow characterization, in particular, shortly before instability occurs. Therefore, the C_s standard deviation is calculated by a moving time average by applying a moving time window of 0.4 FTT (corresponding to 2000 iterations). In other words, the standard deviation at time t is calculated based on the last 2000 iterations. Figure 11 shows the time histories and C_s standard deviations at the probe point P3 (see Fig. 6) on the LHS from the simulation start to 3 FTT (corresponding to 15 000 iterations), and on the RHS, for the period between 2.1 and 2.7 FTT. The upper row shows both C_s fluctuations and standard deviations. For clarity purposes, the lower row shows only the standard deviations.

First, we compare the two stable LDMK-CC-0.02 and LDMK-CC-0.05. Their standard deviations become approximately stationary after 2.0 FTT (10 000 iterations). At 2.6 FTT, the LDMK-CC-0.02 and LDMK-CC-0.05 standard deviations are about 0.017 and 0.023, respectively. So there is a 35% standard deviation difference between the two models. This standard deviation difference can be explained as follows. In the period 2.2–2.6 FTT (2000 iterations), the LDMK-CC-0.05 produces about 800 fluctuations (40%) with $|C_s| \geq 0.02$: 450 negative and 350 positive fluctuations. On the other hand, the LDMK-CC-0.02 has about 220 fluctuations (11%) with $|C_s| \geq 0.02$ (only positive fluctuations). This difference of relatively large fluctuations then implies the 35% standard deviation differences of the LDMK-CC-0.02 and LDMK-CC-0.05. This comparison makes it also evident that the constant clipping of negative C_s values does not only affect negative C_s fluctuations but also positive C_s fluctuations are affected.

Next, we compare the stable LDMK-CC-0.05 and the unstable LDMK-CC-0.2, which becomes unstable after 2.6 FTT. For 0–2.2 FTT (11 000 iterations), the LDMK-CC-0.2 C_s standard deviation is about the same as the LDMK-CC-0.05 standard deviation: there were only about 400 LDMK-CC-0.2 C_s fluctuations with $|C_s| \geq 0.05$ compared to about 240
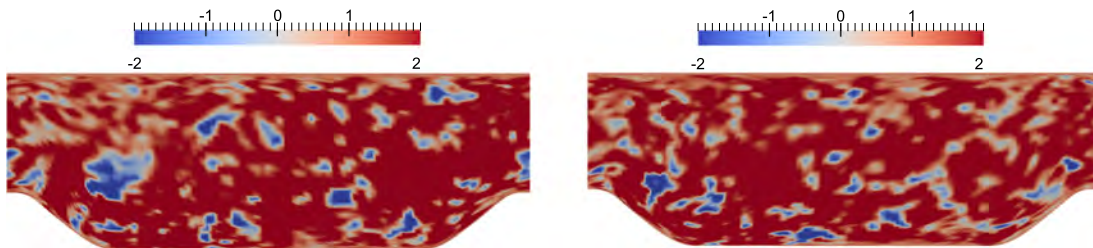
FIG. 10. Snapshots of $(\nu_t + \nu)/\nu$ for the stable LDMK (left) and unstable LDMK-CC-02 models (right). The time step is $\Delta t = 0.002$.
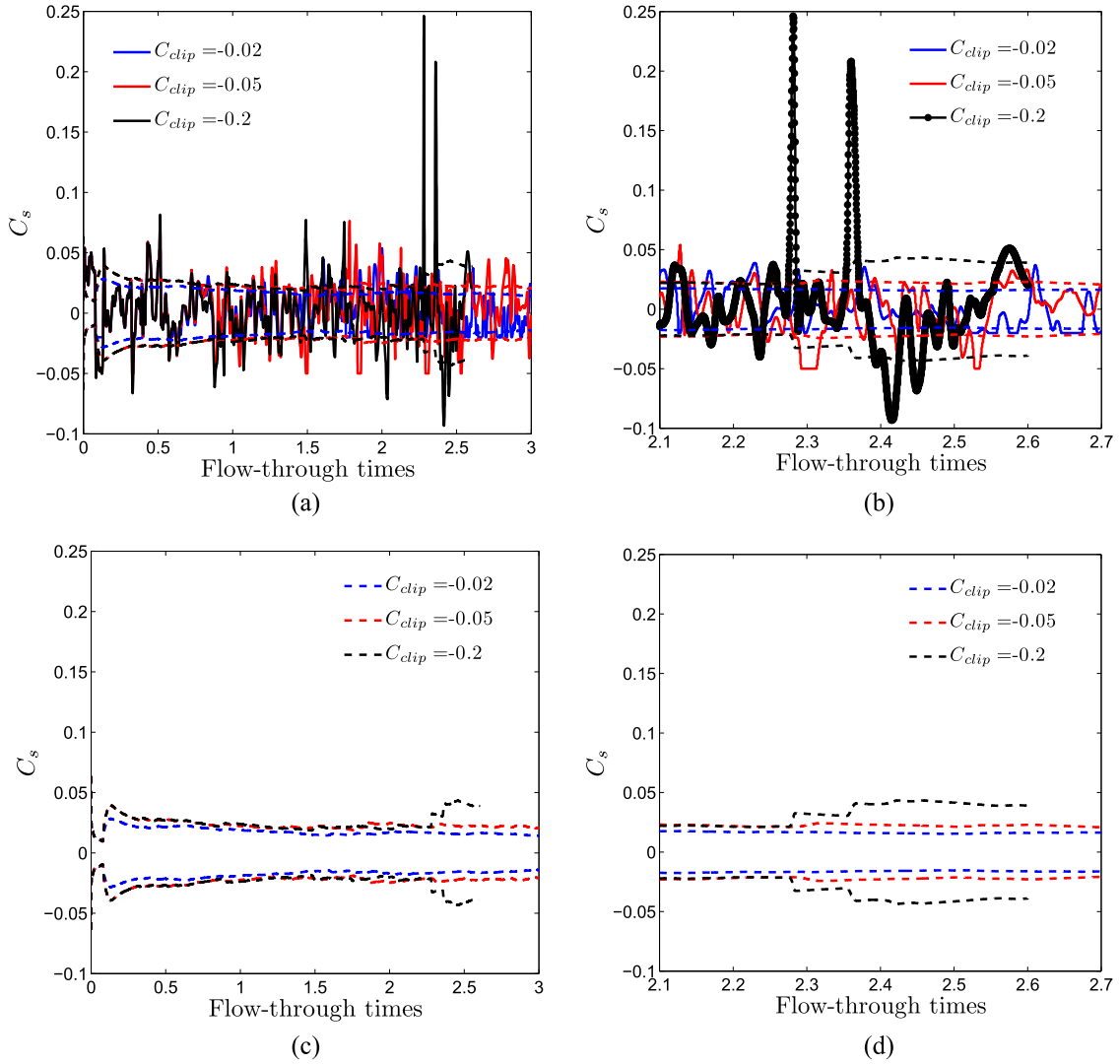
FIG. 11. LDMK-CC C_s time histories and standard deviations (dashed lines, same color) for three clipping constants at P3. The time step is $\Delta t = 0.002$. The last row only shows the standard deviations.

corresponding LDMK-CC-0.05 C_s fluctuations. After 2.2 FTT, the LDMK-CC-0.2 produces a series of big fluctuations with maximum amplitudes of 0.25 and 0.22. For 2.2–2.6 FTT (2000 iterations), the LDMK-CC-0.2 exhibits 300 C_s fluctuations with $|C_s| \geq 0.05$ and 160 C_s fluctuations with $|C_s| \geq 0.08$. It should be noted that there is no fluctuation with $|C_s| \geq 0.08$ before 2.2 FTT. The value of the LDMK-CC-0.2 standard deviation reaches 0.039 before the crash, which corresponds to a 70% C_s standard deviation increase in the 2.2–2.6 FTT period.

By comparing the observations made in the preceding two paragraphs, we see significant differences between stable and unstable models. Stable models are characterized by "noise-type" random C_s variations which imply C_s standard deviation variations that do not vary much in time. On the other hand, on top of "noise-type" random C_s variations, unstable models are characterized by intermittent "outburst", i.e., very large C_s fluctuations that imply sudden jumps of C_s standard deviations to new plateau values. It is of interest to ask why we see, actually, sudden jumps of C_s standard deviations to new plateau values (this observation is not obvious: it could be,

for example, that a higher value of C_{clip} leads to a gradually increasing, slightly higher C_s standard deviation, as seen by comparing the LDMK-CC-0.02 and LDMK-CC-0.05 models).

The latter question is addressed in terms of Fig. 12, which shows the time history and standard deviation of C_s at the probe point P3 for the small period 2.2–2.3 FTT. It can be seen that in this period of time, C_s experiences a big fluctuation that has a maximum value of about 0.25. This big fluctuation takes place over about 100 time steps (0.02 FTT, equivalent to 0.2 s), which is consistent with the correlation in time at the point P3: see Fig. 8(a) in Sec. V. After this big fluctuation, the standard deviation increases to a new plateau value. The reason why the standard deviation rapidly increases to the new plateau value is the relative long correlation of C_s values. For example, if we assume that this big fluctuation would happen two times faster such that it would last 0.1 s (50 time steps), then the new plateau would have a lower value. Or, if we assume a random, uncorrelated distribution of C_s involved in the large fluctuation at about 2.28 FTT over the preceding 2000 time steps, we would not observe a new standard deviation plateau value at
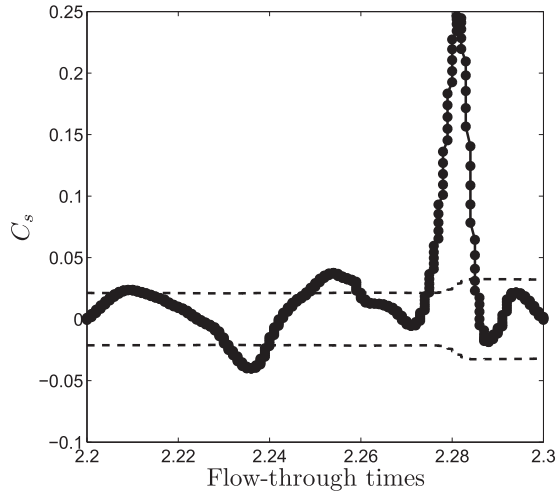
FIG. 12. LDMK-CC-0.2 C_s time history (black symbols) and standard deviation (dashed line) at P3.

2.285 FTT (we would have a smooth transition to new standard deviation values). However, it is relevant to note that the long correlation of C_s is only a factor that contributes to the development of instabilities. In other words, it is not the case that a long correlation of negative C_s values causes instabilities.[12] This view is further supported by considering the correlation of negative C_s values for 2.22–2.25 FTT in Fig. 12, which

takes place over about 150 time steps (0.3 s). This fluctuation does not lead to an abrupt change of the C_s standard deviation, and there is no indication that this fluctuation contributes to the development of instabilities.

C. C_s standard deviation: Imbalances in space

To obtain a more comprehensive view of observations made in Sec. VI B, let us consider the LHS of Fig. 13, which shows for the three models considered contour plots of the C_s standard deviation in the entire flow field averaged over the 2.2–2.6 FTT period. We see again that a higher C_{clip} leads to a higher C_s standard deviation. We also see remarkable differences between stable and unstable models. The stable (LDMK-CC-0.02 and LDMK-CC-0.05) models show relatively smooth C_s standard deviation variations in space. The unstable LDMK-CC-0.2 model produces a very different picture: the relatively smooth red area in the channel center generated by the LDMK-CC-0.05 is enlarged in the LDMK-CC-0.2 case, broken apart into many fine scale structures, and distributed over all the domains. It is interesting to see that spatial correlations are preserved: we still see streak-type, elongated, coherent structures. These features are consistent with the corresponding evolution of the C_s standard deviation in time seen in Fig. 11. In particular, the appearance of intermittent, large C_s fluctuations seen in the unstable model prediction simply reflects a
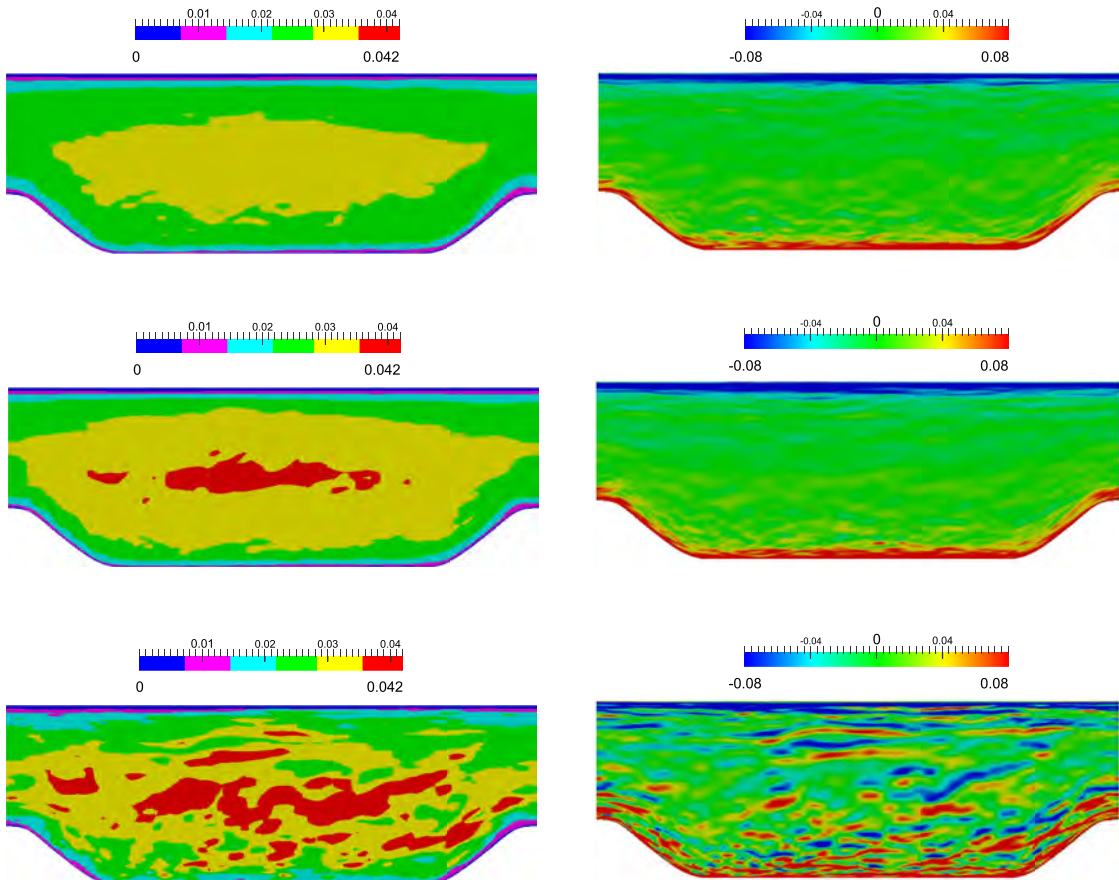
FIG. 13. Contour plots of the C_s standard deviation (left) and its y-gradients $\partial \langle C_s' C_s' \rangle^{1/2} / \partial y$ (right) for the stable LDMK-CC-0.02 (first row), the stable LDMK-CC-0.05 (second row), and the unstable LDMK-CC-0.2 (third row). The time step is $\Delta t = 0.002$.

correlated, high standard deviation structure that passes the point considered.

An even clearer picture of these differences is given on the RHS of Fig. 13, which compares the gradients of C_s standard deviations in the y-direction for the three models considered. The two stable models show relatively smooth distributions of gradients. Large positive and negative gradients are found close to the walls, where C_s changes significantly due to the damping effect of the wall. The positive and negative values of gradients close to the lower and upper walls are related to the direction of the y-axis (for increasing y, we find a C_s standard deviation increase and decrease close to the lower and upper wall, respectively). The unstable model considered shows a different picture. We see streaks of positive and negative gradients distributed over all the domains. The streak organization follows the well-known boundary layer features: positive streaks are followed by negative streaks and vice versa. One interesting aspect of this distribution is that correlations are clearly preserved, we do have elongated, coherent streaks and not a purely random distribution of areas of low and high gradients. Another interesting aspect of this distribution is the significant strength of gradients, which is indicated by red and blue. It turns out that the gradients of streaks are comparable to the very strong gradients seen in the near-wall regions. We will talk about wall-type gradient streaks below if we refer to the strength of C_s standard deviation gradients below. The steady presence of such correlated wall-type gradient streaks (flow imbalances) makes it then impossible for the flow solver to balance these gradients, which finally leads to instability.

The comparison of findings presented in the preceding paragraph with the results obtained regarding the LDMK features enables an alternative explanation of reasons for instability. The LDMK discussion led to the conclusion that instability is caused by non-realizable states. This conclusion can be made more explicit now by stating that instability is caused by the stable spatial organization of significant unphysical states, which are represented by wall-type gradient streaks.

VII. LDMK VERSUS OTHER DYNAMIC MODELS

After discussing the LDMK features and reasons for instability in preceding sections, we will compare the LDMK features with the corresponding features of other dynamic models. Two groups of other models will be considered. First, the LDMK-CC is considered, which represents one of the most common ways to deal with the instability problem. Nevertheless, the LDMK-CC approach is known to be rather problematic because of the unknown knowledge of an appropriate LDMK-CC clipping value. As a simple alternative to the LDMK-CC, we also consider another stabilization approach given by requiring the total viscosity to be positive, i.e., $\nu + \nu_t \geq 0$. We will refer to this model as LDMK-PTV (LDMK with positive total viscosity). The second group of models considered for comparisons focuses on often applied models: equilibrium models that do not involve a subgrid kinetic energy equation. In particular, the equilibrium version LDME of the LDMK and a

stabilized dynamic Smagorinsky model (DSMS) are considered. A major motivation for involving equilibrium models is to consider the possibility of using our dynamic bound approach in conjunction with other, usually applied dynamic models.

The LDMK-PTV, LDME, and DSMS models involved here will be presented in Secs. VII A and VII B. Then, comparisons with respect to the stability and performance of models will be presented in Secs. VII C and VII D.

A. LDMK-PTV

A simple approach to avoid the known issues of dealing with LDMK-CC problems is the enforcement of a positive total viscosity, $\nu + \nu_t \geq 0$, which is known to be an effective mean to stabilize dynamic models. Characteristic features of this LDMK-PTV approach will be described here.

The LHS of Fig. 14 compares the C_s time history for the LDMK-CC-0.02 and LDMK-PTV at the P1 probe point located in the shear layer. At this point, it can be seen that the LDMK-PTV behaves like an LDMK-CC model with a very small effective negative clipping constant approximately given by $C_{clip} = -0.015$. Unlike the LDMK-CC, which applies a constant clipping with respect to the entire flow field, the LDMK-PTV applies a local clipping $C_{clip} = -\nu/(k\tau)$ according to $\nu + C_{clip}k\tau \geq 0$. So it could be that the LDMK-PTV behaves very differently from the LDMK-CC-0.02 in other points as considered on the LHS of Fig. 14. This question is addressed in terms of the RHS of Fig. 14, which shows C_s snapshots for the entire flow field. The similarity of C_s distributions of the LDMK-CC-0.02 and LDMK-PTV also supports the view that the LDMK-PTV model behaves like an LDMK-CC with a rather small negative clipping constant.

Compared to the LDMK-CC, an advantage of the LDMK-PTV is that the LDMK-PTV does not need a tuning of C_{clip}. A disadvantage of the LDMK-PTV is the following. The term $\nu/(k\tau)$ in $C_{clip} = -\nu/(k\tau)$ represents an inverse turbulence Reynolds number, i.e., the RHS in $C_{clip} = -\nu/(k\tau)$ approaches zero for very high Reynolds number flows. Thus, only a very small (or almost zero) amount of negative C_s values is allowed in the LDMK-PTV model concept for high Reynolds numbers, i.e., this model is hardly able to account for the relevant backscatter.[68,69] As a consequence of the similarity between the LDMK-PTV and LDMK-CC and the lack of alternative provided by the LDMK-PTV, we will not further consider the LDMK-PTV.

B. LDME and DSMS

An equilibrium version of the LDMK, which does not require the solution of a transport equation for k, can be obtained in the following way. According to Eq. (10), we equate the last two terms, this means we assume that the production is balanced by the dissipation. This implies

$$k = C_* \Delta^2 |\widetilde{S}|^2, \tag{31}$$

where $C_* = 2(1 - c_0)/3$. By using this expression in $\nu_t = 2(1 - c_0)/3 k^{1/2}\Delta$, we obtain an equilibrium deterministic SGS stress model given by

$$\nu_t = C_e \Delta^2 |\widetilde{S}|, \tag{32}$$
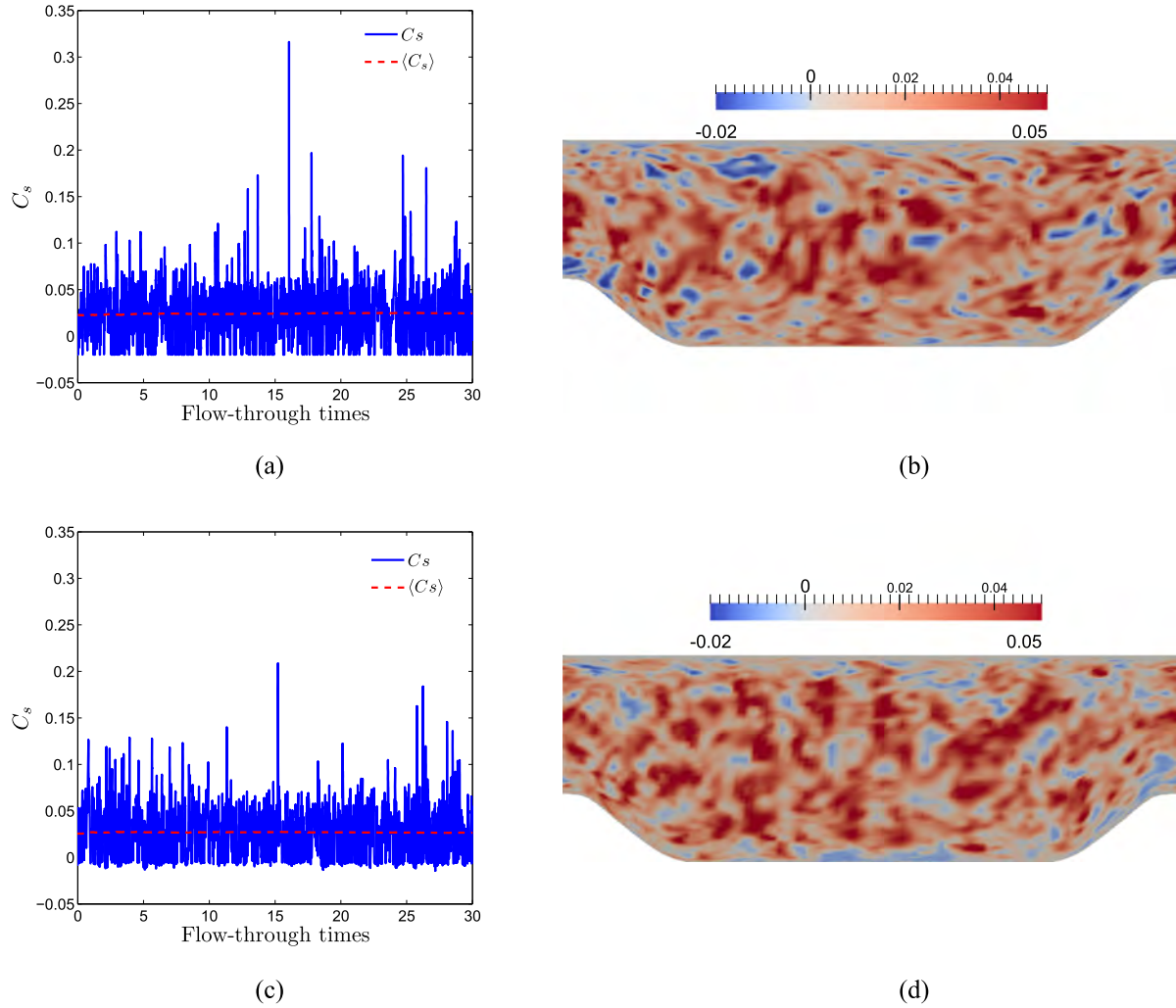
FIG. 14. LDMK-CC-0.02 and LDMK-PTV time histories of C_s at P1 (left) and C_s snapshots (right). The time step is $\Delta t = 0.002$. (a) LDMK-CC-0.02, (b) LDMK-CC-0.02, (c) LDMK-PTV, and (d) LDMK-PTV.

where $C_e = [2(1 - c_0)/3]^{3/2}$. The use of $c_0 = 0.86$ implies $\nu_t = 0.17^2\Delta^2|\overline{S}|$, which is equivalent to the standard Smagorinsky model.

However, as given with respect to the LDMK, it is highly beneficial to dynamically calculate C_e. The approach to obtain such a dynamic model follows the approach to derive the corresponding LDMK expression. The stochastic analysis approach provides $L_{ij}^d = -2C_e(\Delta^T)^2|\widetilde{\overline{S}}|\widetilde{\overline{S}}_{ij}$ for the deviatoric component L_{ij}^d of the Leonard stress, corresponding to the deviatoric SGS stress $\tau_{ij}^d = -2C_e\Delta^2|\widetilde{S}|\widetilde{S}_{ij}$ implied by Eq. (32). By introducing the abbreviation $m_{ij} = 2(\Delta^T)^2|\widetilde{\overline{S}}|\widetilde{\overline{S}}_{ij}$, the Leonard stress expression can also be written $L_{ij}^d = -C_e m_{ij}$. Then, the setting

$$C_e = -\frac{L_{ij}^d m_{ji}}{m_{kl}m_{lk}} \quad (33)$$

can be shown to the minimize the least squares error related to C_e settings. Formally, Eq. (33) is equivalent to multiplying $L_{ij}^d = -C_e m_{ij}$ with m_{ij}. The model equation (33) will be referred to as LDME referring to the equilibrium LDMK.

The problem related to using the dynamic bounds approach presented in Sec. II for the case here is that k is

unavailable because no k equation is involved. The way to overcome this problem is to consider $k^T = C_*(\Delta^T)^2|\widetilde{\overline{S}}|^2$, corresponding on the test filter level to $k = C_*\Delta^2|\widetilde{S}|^2$. The ratio k/k^T reads then

$$\frac{k}{k^T} = \frac{\Delta^2|\widetilde{S}|^2}{(\Delta^T)^2|\widetilde{\overline{S}}|^2}. \quad (34)$$

Expression (34) generalizes the usual assumption that k and k^T are proportional to each other, where the proportionality coefficient is considered to be constant.[7,70,71] It is worth noting that k defined in this way is nonnegative by definition. The latter represents a serious problem if the Germano dynamic concept[72] is applied.[36] According to the realizability condition $|\nu_t^*| \leq 23/48$ derived in Sec. II combined with $\nu_t = C_e\Delta^2|\widetilde{S}|$, the stress realizability condition for the LDMKE is given by

$$|C_e| \leq \frac{23}{24\sqrt{3}}\frac{k}{\Delta^2|\widetilde{S}|^2} = \frac{23}{24\sqrt{3}}\frac{k^T}{(\Delta^T)^2|\widetilde{\overline{S}}|^2}, \quad (35)$$

where Eq. (34) was applied.

Next, we consider the original dynamic Smagorinsky model, which will be stabilized by using our dynamic bound approach. This model applies an equilibrium expression for k

in the SGS viscosity ν_t leading to $\nu_t = C_e \Delta^2 |\widetilde{S}|$, where C_e is obtained via

$$C_e = -\frac{L_{ij}^d H_{ij}}{H_{mn} H_{mn}}. \tag{36}$$

Here, the expression H_{ij} is given by

$$H_{ij} = 2 \left(\Delta^T\right)^2 |\overline{\widetilde{S}}| \overline{\widetilde{S}}_{ij} - 2\Delta^2 \overline{|\widetilde{S}| \widetilde{S}_{ij}}. \tag{37}$$

According to the results given above, see Eq. (35), C_e is dynamically bounded by

$$|C_e| \leq \frac{23}{24\sqrt{3}} \frac{k^T}{(\Delta^T)^2 |\overline{\widetilde{S}}|^2}. \tag{38}$$

Let us comment on this approach. First, it was shown that the original DSM is not supported by a theory based derivation of dynamic models.[24,25] The theory based approach implies Eq. (33) for C_e, which differs from the original DSM. The difference given by Eq. (33), basically, avoids the developments of numerical instabilities. Second, the main motivation of involving the DSM in this model comparison was to consider the possibility to transfer the dynamic bound concept presented here to other dynamic eddy-viscosity type models, in particular models that apply an equilibrium expression for the subgrid kinetic energy k. The popular DSM is used as an example for such a model.

C. LDMK-CC, LDME, and DSMS comparison: Stability

After introducing the LDME and DSMS in Sec. VII B and excluding the LDMK-PTV from further comparisons in Sec. VII A, we focus now on the comparison of the LDMK-CC, LDME, and DSMS with respect to their stability, this means we consider the conditions under which it is possible to finish simulations. The stability of the LDMK was already discussed in Sec. IV.

First, we consider the LDMK-CC. It needs the specification of a non-zero C_{clip}: the setting $C_{clip} = 0$ cannot be seen

TABLE II. LDMK-CC (using different C_{clip}), LDME, and DSMS stability analysis for different Δt.

Simulation	$\Delta t = 0.001$	$\Delta t = 0.002$	$\Delta t = 0.004$	$\Delta t = 0.008$	$\Delta t = 0.01$
LDMK-CC-0.02	Stable	Stable	Stable	Stable	Stable
LDMK-CC-0.05	Stable	Stable	Stable	Stable	Stable
LDMK-CC-0.075	Stable	Unstable	Unstable	Unstable	Unstable
LDMK-CC-0.2	Unstable	Unstable	Unstable	Unstable	Unstable
DSMS-1B	Unstable	Unstable	Unstable	Unstable	Unstable
DSMS-0.5B	Stable	Stable	Stable	Stable	Stable
LDME-1B	Unstable	Unstable	Unstable	Unstable	Unstable
LDME-0.5B	Stable	Stable	Stable	Stable	Stable

to be an attractive alternative because it excludes the relevant backscatter. Unfortunately, it turns out that the specification of an appropriate, not too small C_{clip} is a rather difficult problem: the choice of appropriate C_{clip} values depends on the type of flow, Reynolds number, the simulation time step, and grid resolution. An illustration of these problems is given in Table II, which summarizes the stability analysis of different LDMK-CC models. For $C_{clip} = -(0.02, 0.05)$, we see that the LDMK-CC model is stable for a wide range of time steps ranging from 10^{-3} to 10^{-2}, which corresponds to CFL numbers ranging from 0.1 to 0.8. For $C_{clip} = -0.075$, the LDMK-CC is only stable for the smallest time step, and the LDMK-CC is unstable for all time steps for $C_{clip} = -0.2$.

Table II also presents the DSMS and LDME stability analysis results. It was surprising that both the DSMS-1B and LDME-1B turned out to be unstable. In particular, the LDME-1B and DSMS-1B became unstable after 7.5 and 2.5 FTT, respectively. Stability of both these models for a wide range of time steps was accomplished if these models were used with half bounds, this means as LDME-0.5B and DSMS-0.5B. In this regard, it has to be noted that the realizability bounds for both the LDME and DSMS do not exactly represent realizability bounds, but they have to be considered as approximations to the real bounds (which are unknown because of the missing knowledge of the subgrid kinetic energy).
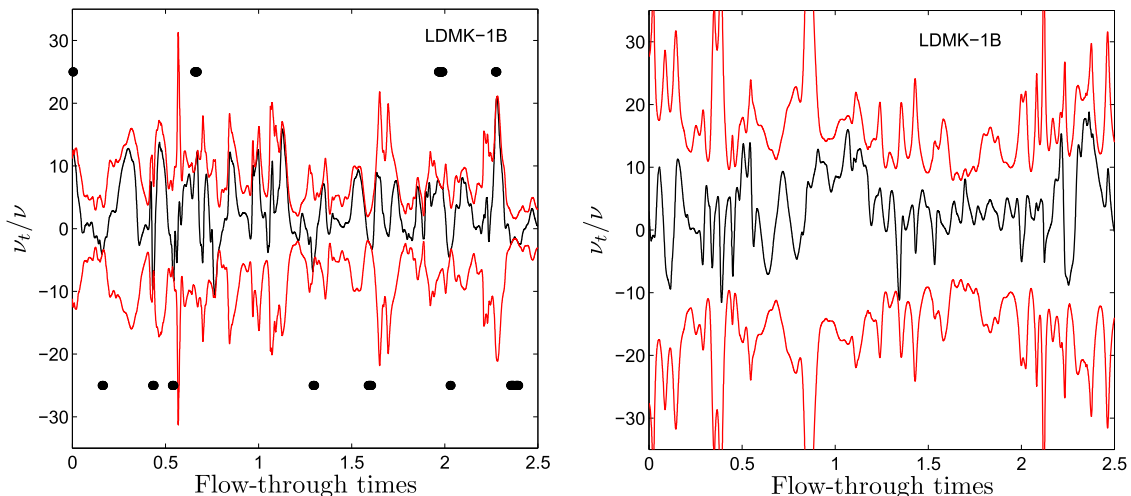
FIG. 15. LDMK time histories of the eddy viscosity ratio (black lines) at P1 (left) and P2 (right). Red lines show the realizability bounds and black circles show the time at which ν_t hits the realizability bounds. The time step is $\Delta t = 0.001$.

D. LDMK-CC, LDME, and DSMS comparison: Performance

The next step is to obtain insight into the performance of LDMK-CC, LDME, and DSMS models in simulations. It turned out that there were no significant differences between different dynamic models with respect to the calculation of mean velocities and Reynolds stresses. One option to obtain further insight into model features would be the comparison of backscatter. We did this and saw that the DSMS produces (in contrast to the other models) significant backscatter peaks close to the wall. However, the evaluation of these features suffers from missing data for comparisons. Thus, to illustrate model performance differences, we decided to focus on the
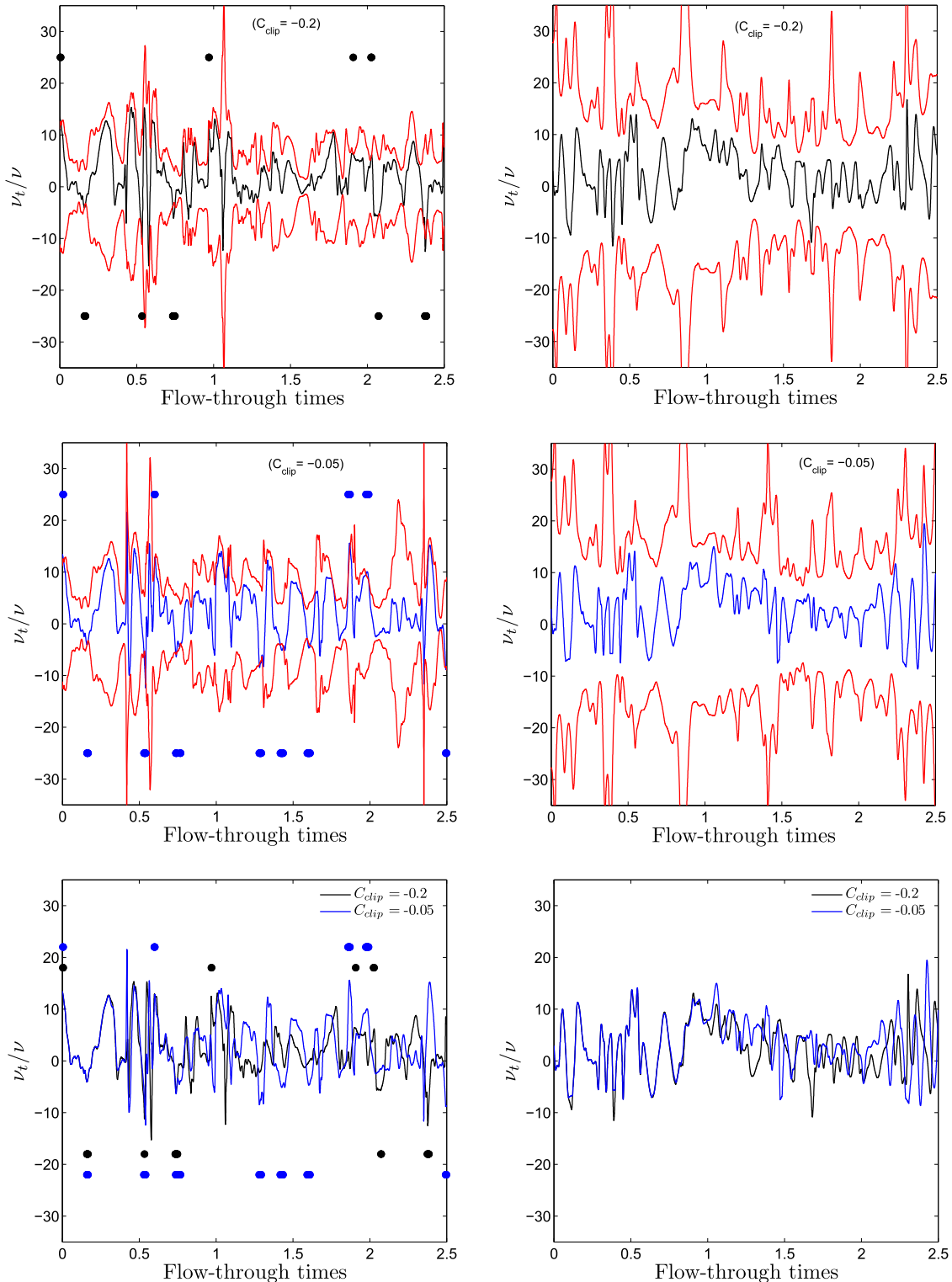
FIG. 16. Unstable LDMK-CC-0.2 (black lines) and stable LDMK-CC-0.05 (blue lines) eddy viscosity ratios at P1 (left) and P2 (right). Circles in corresponding colors (blue and black, respectively) show the times at which ν_t/ν hits the bounds. Red lines show the bounds. The time step is $\Delta t = 0.001$.

real difference of models in simulations: the instantaneous sub-grid viscosity, which we consider normalized to the constant kinematic viscosity.

We considered a time period of 2.5 FTT because the DSMS-1B model becomes unstable after this time.

Corresponding plots of the stable LDMK, the unstable LDMK-CC-0.2 and stable LDMK-CC-0.05, the unstable LDME-1B and stable LDME-0.5B, the unstable DSMS-1B and stable DSMS-0.5B are shown in Figs. 15–18, respectively, at probe points P1 and P2. Table III provides the hitting probabilities
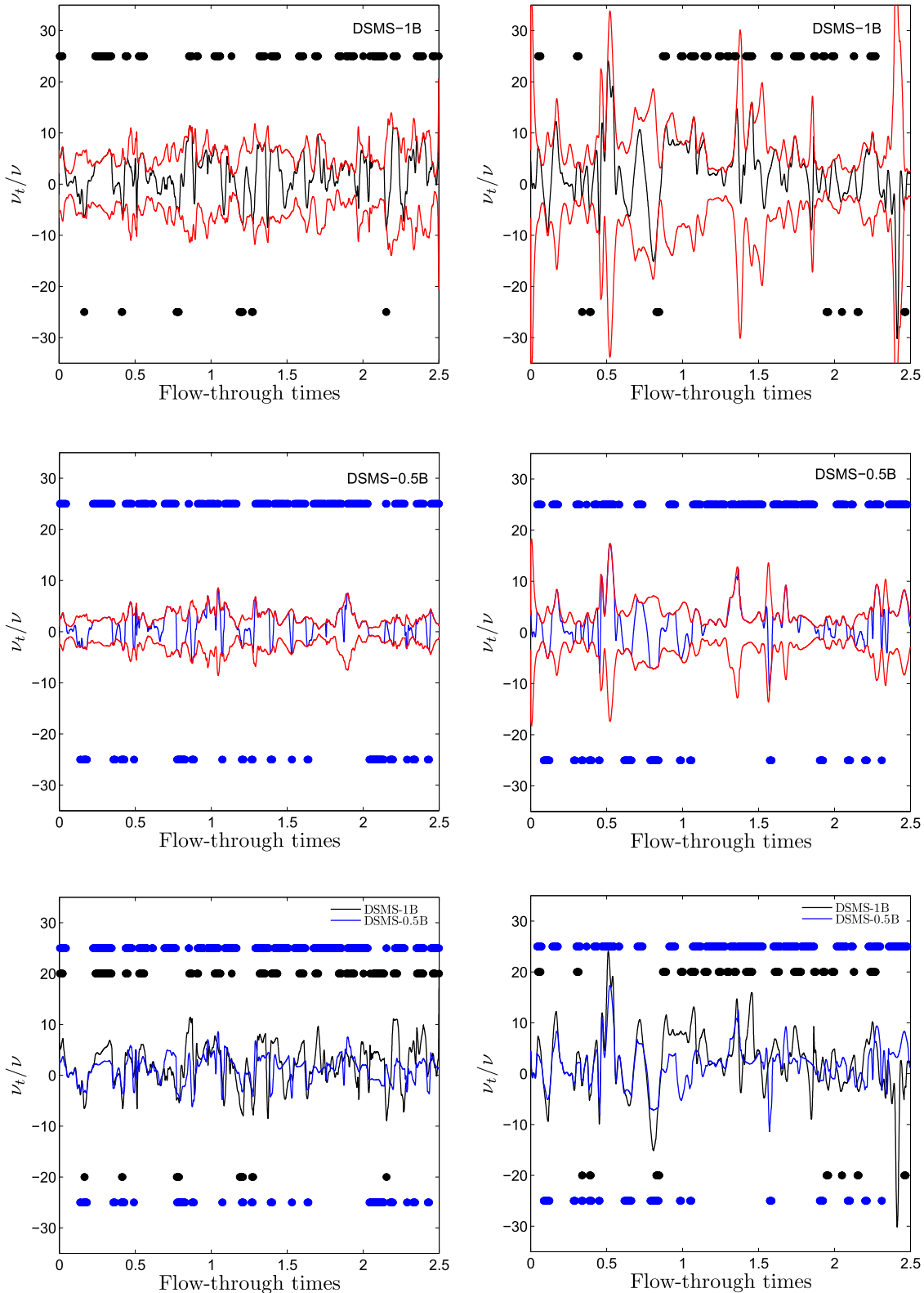
FIG. 17. Unstable DSMS-1B (black lines) and stable DSMS-0.5B (blue lines) eddy viscosity ratios at P1 (left) and P2 (right). Circles in corresponding colors (blue and black, respectively) show the times at which ν_t/ν hits the bounds. Red lines show the bounds. The time step is $\Delta t = 0.001$.
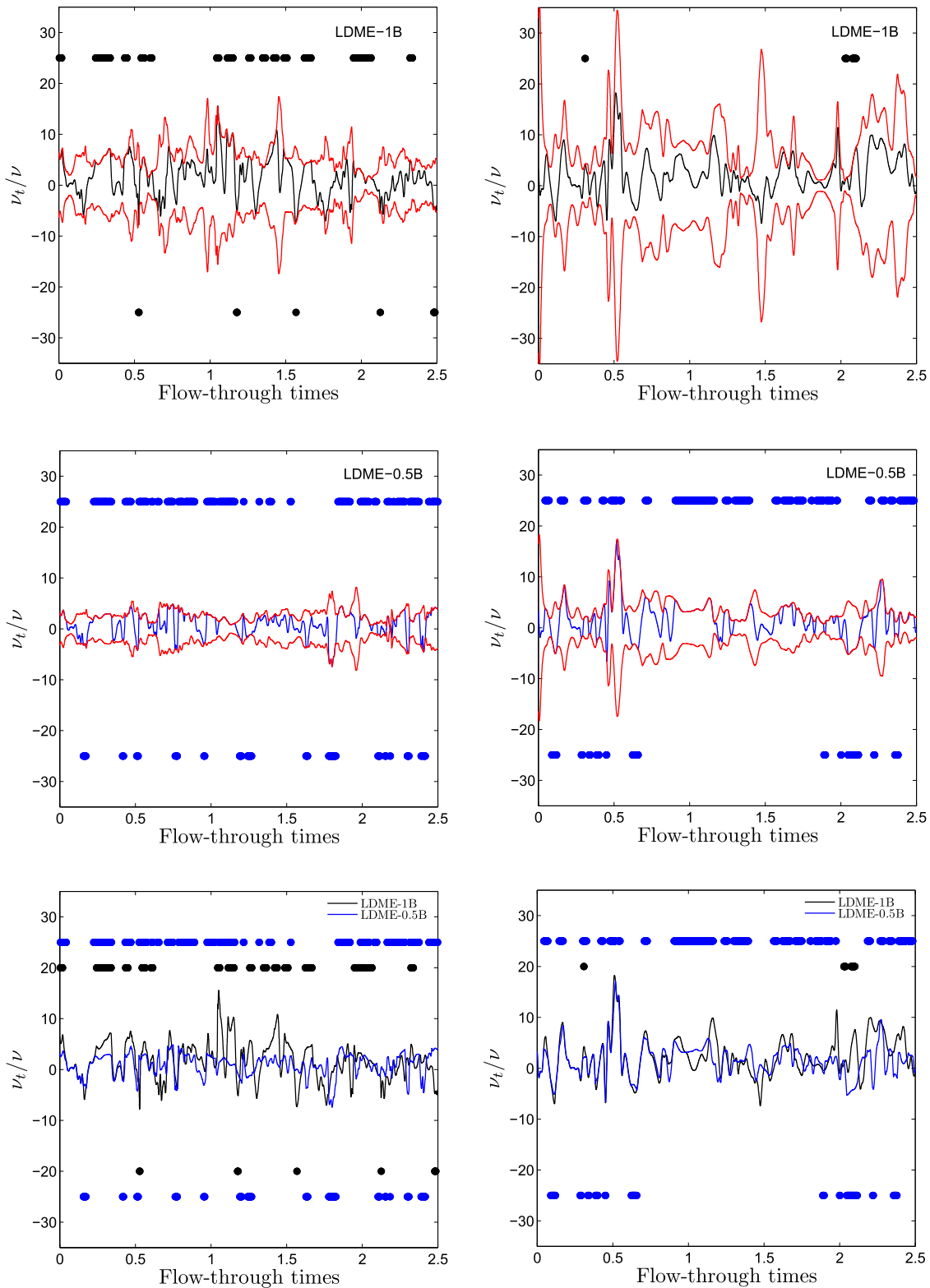
FIG. 18. Unstable LDME-1B (black lines) and stable LDME-0.5B (blue lines) eddy viscosity ratios at P1 (left) and P2 (right). Circles in corresponding colors (blue and black, respectively) show the times at which ν_t/ν hits the bounds. Red lines show the bounds. The time step is $\Delta t = 0.001$.

of realizability bounds of these models at P1 and P2. The hitting probabilities are calculated for 2.5 FTT corresponding to 25 000 iterations.

The comparison of the LDMK with the LDMK-CC shows that ν_t/ν and its bounds behave very similar: the range of variations is approximately the same. Overall, these curves

correspond to expectations for a clipping, the clipping should not imply significant changes of variations considered but only provide relatively minor limitations. For the time period considered, there is no obvious difference between unstable LDMK-CC-0.2 and stable LDMK-CC-0.05 variations. A closer look shows that the LDMK-CC concept gives room for

TABLE III. LDMK, LDME, and DSMS hitting probabilities at P1 and P2: HP⁻ (HP⁺) refer to negative (positive) bound hittings.

Simulation	HP_{P1}^-	HP_{P1}^+	HP_{P2}^-	HP_{P2}^+
LDMK-1B	0.03	0.02	0	0
DSMS-1B	0.03	0.25	0.03	0.16
DSMS-0.5B	0.15	0.52	0.12	0.47
LDME-1B	0.01	0.17	0	0.02
LDME-0.5B	0.08	0.38	0.09	0.36

the existence of very strong non-equilibrium states represented by significant peaks in the bound curves (see in particular, the P1 curves), which are not seen in the corresponding LDMK model curves. It is plausible that such strong non-equilibrium states may be the reason for instabilities: depending on the impact of these v_t/v bound peaks, this fact may explain the sensitivity of the LDMK-CC stability to choosing the clipping parameter.

The comparison of the LDMK with the unstable DSMS-1B reveals the significant reduction of the range of dynamic v_t/v variations given by the much more restrictive DSMS bounds. The use of the stable DSMS-0.5B further restricts the range of v_t/v variations significantly. It turns out that the need to stabilize the model via the use of half bounds has significant consequences for the dynamic v_t/v variation. The DSMS-0.5B curves show that there are extended periods of time where the v_t/v variation is equal to the corresponding bound variation. This means that the dynamic model parameter calculation via minimizing the local error does not work anymore. Hence, v_t/v is calculated on an unphysical basis. The direct comparison of DSMS-1B and DSMS-0.5B curves also does not support this approach. As argued above regarding the LDMK-CC discussion, the use of a clipping (as given by using half bounds) should not imply drastic changes of v_t/v variations. However, the latter is the case, as may be seen in the last row of Fig. 17. Table III quantifies these observations. This table shows, for example, that at both P1 and P2, the stable DSMS-0.5B implies a probability of upper bound hittings of about 50%. This means, v_t/v variations are substantially governed by the bound variations, which is in contrast to the dynamic modeling concept applied. Overall, the use of Eq. (38) in conjunction with the DSM cannot be recommended.

There may be two reasons for the DSMS shortcomings, the behavior of the DSMS can be caused by the known shortcomings of the DSM concept, or, it can be caused by the approximation applied to provide an equilibrium value for the subgrid kinetic energy. This question can be addressed by considering the corresponding behavior of the LDME shown in Fig. 18. We see that the range of v_t/v variations allowed by the bounds is less restrictive than the corresponding range of the DSMS. However, compared to the LDMK, there is still a significant restriction of v_t/v variations. Similar to the DSMS model behavior, we see that there are extended periods of time where the v_t/v variation is equal to the corresponding bound variation. The direct comparison of LDME-1B and LDME-0.5B curves shows advantages compared to the DSMS: we see that the bounding does not have a very strong effect on v_t/v variations. The comparison of DSMS and

LDME hitting probabilities given in Table III also supports the view that the LDME has advantages compared to the DSMS (for example, the probability of upper bound hittings implied by the LDME-0.5B is clearly reduced compared to the DSMS case). Overall, however, the significant reduction of v_t/v variations compared to the LDMK in conjunction with unphysical variations of v_t/v over extended periods of time do not provide support for the use of Eq. (38) in conjunction with the LDME. Therefore, first of all, the DSMS and LDME problems reported here indicate that the reason for these shortcomings is given by the use of the k approximation equation (34). In other words, the use of exact local realizability conditions via the calculation of k has clear advantages compared to the use of approximations for k.

VIII. SUMMARY AND CONCLUSIONS

PDF-realizable dynamic LES models can be derived from an underlying stochastic model for turbulent velocities. Such dynamic LES are proven to have significant advantages compared to the models that do not honor realizability constraints.[24–26,28] In previous applications to turbulent channel flows and the turbulent Ekman layer, such models enabled stable simulations without the need for clipping or averaging dynamic model parameters.[25,26] However, with respect to more complex flows, it was found that such dynamic models are not always computationally stable.[28] To overcome this problem, a local dynamic bounding of model parameters, which ensures the realizability of the SGS stress tensor, was derived and tested here. The main result derived is the conclusion that a PDF-realizable model which involves the calculation of the subgrid kinetic energy is computationally stable if it is also stress-realizable. On the other hand, a model that is not stress-realizable can become unstable.

We considered reasons for instability in order to better understand why realizability and stability are closely related to each other. It was assumed previously that long-term correlations of negative dynamic model parameters are responsible for instability.[12] We did not find support for this view: we concluded that strong imbalances of C_s standard deviations in space and time (which are excluded if the model is stress-realizable) imply instabilities. In particular, we concluded that instability is caused by the stable spatial organization of significant unphysical states, which are represented by wall-type gradient streaks.

We also compared the stress-realizable dynamic model obtained with other dynamic LES models. The option to combine our dynamic LES model with a constant clipping (which corresponds to the use of the LDMK-CC) was found to be little attractive. For a certain choice of the clipping constant, the LDMK-CC has unpredictable stability properties because of the production of strong non-equilibrium states (bound peaks). The LDMK-PTV, which ensures a positive total viscosity, was identified to be equivalent to a LDMK-CC which only allows small negative dynamic parameter values: so this model does not offer a promising alternative. We also discussed the transfer of our dynamic bounding approach to equilibrium models that do not solve for the subgrid kinetic energy: we considered the equilibrium version of our LDMK (the LDME) and DSM

stabilized in this way (the DSMS). Although the models perform differently (the LDME offers clear advantages compared to the DSMS), our conclusion was that these bounded equilibrium models cannot perform in a comparable way than the LDMK: they suffer from a significant reduction of subgrid viscosity bounds and unphysical bound calculations for extended periods of time. The reason for that is the algebraic approximation for the subgrid kinetic energy, which introduces local imbalances.

Our overall conclusion is the following. We may consider optimal dynamic LES as having at least the following properties. First, such LES should be local in physical space without involving artificial information (artificial clipping parameters or correlations, see the third paragraph of the Introduction). Second, such LES should be stable for a wide range of simulation time steps, Reynolds numbers, and numerical schemes. These properties are not trivial, but dynamic LES suffers from problems with these properties over decades. The main result of our studies is that it is possible to design such LES. It requires a strict physical consistency: a PDF-realizable and stress-realizable LES model. Here, strict stress-realizability requires the inclusion of the subgrid kinetic energy in the LES calculation. LES models that do not honor such strict physical consistency can become unstable.

ACKNOWLEDGMENTS

[1] C. Meneveau, "Statistics of turbulence subgrid-scale stresses: Necessary conditions and experimental tests," Phys. Fluids **6**(2), 815–833 (1994).

[2] P. J. Mason, "Large-eddy simulation: A critical review of the technique," Q. J. R. Meteorol. Soc. **120**(515), 1–26 (1994).

[3] M. Germano, "Fundamentals of large eddy simulation," in *Advanced Turbulent Flows Computations*, CISM Courses and Lectures Vol. 395, edited by R. Peyret and E. Krause (Springer, Berlin, Heidelberg, New York, 2000), pp. 81–130.

[4] U. Piomelli, "Large-eddy simulation: Achievements and challenges," Prog. Aerosp. Sci. **35**(4), 335–362 (1999).

[5] S. B. Pope, *Turbulent Flows* (Cambridge University Press, Cambridge, 2000).

[6] C. Meneveau and J. Katz, "Scale-invariance and turbulence models for large-eddy simulation," Annu. Rev. Fluid Mech. **32**(1), 1–32 (2000).

[7] P. Sagaut, *Large Eddy Simulation for Incompressible Flows: An Introduction* (Springer-Verlag, Berlin, Heidelberg, New York, Tokyo, 2002).

[8] M. Lesieur, O. Metais, and P. Comte, *Large-Eddy Simulations of Turbulence* (Cambridge University Press, Cambridge, 2005).

[9] M. Germano, U. Piomelli, P. Moin, and W. Cabot, "A dynamic subgrid-scale eddy viscosity model," Phys. Fluids A **3**(7), 1760–1765 (1991).

[10] D. K. Lilly, "A proposed modification of the germano subgrid-scale closure method," Phys. Fluids A **4**(3), 633–635 (1992).

[11] C. Meneveau, T. S. Lund, and W. H. Cabot, "A Lagrangian dynamic subgrid-scale model for turbulence," J. Fluid Mech. **319**, 353–385 (1996).

[12] T. Lund, S. Ghosal, and P. Moin, "Numerical experiments with highly variable eddy viscosity model," in *Engineering Applications of Large Eddy Simulations*, edited by S. A. Ragale and U. Piomelli (ASME, 1993), FED Vol. 162, pp. 7–11.

[13] S. Ghosal, T. S. Lund, P. Moin, and K. Akselvoll, "A dynamic localization model for large-eddy simulation of turbulent flows," J. Fluid Mech. **286**, 229–255 (1995).

[14] U. Piomelli, T. A. Zang, C. G. Speziale, and M. Y. Hussaini, "On the large-eddy simulation of transitional wall-bounded flows," Phys. Fluids A **2**, 257–265 (1990).

[15] U. Piomelli and J. Liu, "Large-eddy simulation of rotating channel flows using a localized dynamic model," Phys. Fluids **7**, 839–848 (1995).

[16] S. Krajnovic and L. Davidson, "Large-eddy simulation of the flow around a bluff body," AIAA J. **40**(5), 927–936 (2002).

[17] S. Krajnovic and L. Davidson, "Large-eddy simulation of the flow around simplified car model," SAE Paper 01–0227, 2004.

[18] A. E. Tejada-Martinez and K. Jansen, "A dynamic Smagorinsky model with dynamic determination of the filter width ratio," Phys. Fluids **16**, 2514–2528 (2004).

[19] L. Marstorp, G. Brethouwer, and A. V. Johansson, "A stochastic subgrid model with application to turbulent flow and scalar mixing," Phys. Fluids **19**(3), 035107-1–035107-12 (2007).

[20] Y. Shi, Z. Xiao, and S. Chen, "Constrained subgrid-scale stress model for large eddy simulation," Phys. Fluids **20**, 011701-1–011701-4 (2008).

[21] N. Park and K. Mahesh, "Reduction of the germano-identity error in the dynamic Smagorinsky model," Phys. Fluids **21**, 065106-1–065106-16 (2009).

[22] W. W. Kim and S. Menon, "A new dynamic one-equation subgrid-scale model for large eddy simulations," AIAA Paper No. 95-356, 1995.

[23] B. C. Wang and D. J. Bergstrom, "A dynamic nonlinear subgrid-scale stress model," Phys. Fluids **17**, 035109-1–035109-17 (2005).

[24] S. Heinz, "Realizability of dynamic subgrid-scale stress models via stochastic analysis," Monte Carlo Methods Appl. **14**(4), 311–329 (2008).

[25] S. Heinz and H. Gopalan, "Realizable versus non-realizable dynamic subgrid-scale stress models," Phys. Fluids **24**(11), 115105-1–115105-23 (2012).

[26] E. Kazemi and S. Heinz, "Dynamic large eddy simulations of the Ekman layer based on stochastic analysis," Int. J. Nonlinear Sci. Numer. Simul. **17**, 77–98 (2016).

[27] S. Heinz, "Turbulent supersonic channel flow: Direct numerical simulation and modeling," AIAA J. **44**, 3040–3050 (2006).

[28] R. Mokhtarpoor, S. Heinz, and M. Stoellinger, "Dynamic unified RANS-LES simulations of high Reynolds number separated flows," Phys. Fluids **28**, 095101-1–095101-36 (2016).

[29] J. Bredberg, S. H. Peng, and L. Davidson, "An improved k-ω turbulence model applied to recirculating flows," Int. J. Heat Fluid Flow **23**(6), 731–743 (2002).

[30] H. Gopalan, S. Heinz, and M. Stöllinger, "A unified RANS-LES model: Computational development, accuracy and cost," J. Comput. Phys. **249**, 249–274 (2013).

[31] Y. Zang, R. L. Street, and J. R. Koseff, "A dynamic mixed subgrid-scale model and its application to turbulent recirculating flows," Phys. Fluids **5**(12), 3186–3196 (1993).

[32] H. Zhao and P. R. Voke, "A dynamic subgrid-scale model for low-Reynolds number channel flow," Int. J. Numer. Methods Fluids **23**(1), 19–27 (1996).

[33] K. Akselvoll and P. Moin, "Large eddy simulation of a backward facing step flow," in *Engineering Turbulence Modelling and Experiments 2*, edited by W. Rodi and F. Martelli (Elsevier Science Publishers, 1993), pp. 303–313.

[34] U. Schumann, "Realizability of Reynolds-stress turbulence models," Phys. Fluids **20**, 721–725 (1977).

[35] P. A. Durbin and C. G. Speziale, "Realizability of second-moment closure via stochastic analysis," J. Fluid Mech. **280**, 395–407 (1994).

[36] B. Vreman, B. Geurts, and H. Kuerten, "Realizability conditions for the turbulent stress tensor in large-eddy simulation," J. Fluid Mech. **278**, 351–362 (1994).

[37] S. S. Girimaji, "A new perspective on realizability of turbulence models," J. Fluid Mech. **512**, 191–210 (2004).

[38] A. Andrén, "Evaluation of a turbulence closure scheme suitable for air-pollution applications," J. Appl. Meteorol. **29**(3), 224–239 (1990).

[39] H. A. Wouters, T. W. J. Peeters, and D. Roekaerts, "On the existence of a generalized Langevin model representation for second-moment closures," Phys. Fluids **8**(7), 1702–1704 (1996).

[40] B. Merci, C. De Langhe, J. Vierendeels, and E. Dick, "A quasi-realizable cubic low-Reynolds eddy-viscosity turbulence model with a new dissipation rate equation," Flow, Turbul. Combust. **66**(2), 133–157 (2001).

[41] T. S. Park and H. J. Sung, "Development of a near-wall turbulence model and application to jet impingement heat transfer," Int. J. Heat Fluid Flow **22**(1), 10–18 (2001).

[42] J. R. Ristorcelli, J. L. Lumley, and R. Abid, "A rapid-pressure covariance representation consistent with the Taylor-Proudman theorem materially frame indifferent in the two-dimensional limit," J. Fluid Mech. **292**, 111–152 (2006).

[43] S. Heinz, "On Fokker–Planck equations for turbulent reacting flows. Part 2. Filter density function for large eddy simulation," Flow, Turbul. Combust. **70**(1), 153–181 (2003).

[44] S. Heinz, *Statistical Mechanics of Turbulent Flows*, 1st ed. (Springer-Verlag, Berlin, Heidelberg, New York, Tokyo, 2003).

[45] S. Heinz, "Comment on 'A dynamic nonlinear subgrid-scale stress model,'" Phys. Fluids **17**, 099101-1–099101-2 (2005).

[46] S. Heinz, "Unified turbulence models for LES and RANS, FDF and PDF simulations," Theor. Comput. Fluid Dyn. **21**(2), 99–118 (2007).

[47] M. Ida and N. Taniguchi, "Can a numerically stable subgrid-scale model for turbulent flow computation be ideally accurate?: A preliminary theoretical study for the Gaussian filtered Navier-Stokes equations," Phys. Rev. E **68**, 036705-1–036705-6 (2003).

[48] M. Ida and N. Taniguchi, "Underlying mechanism of numerical instability in large-eddy simulation of turbulent flows," Phys. Rev. E **69**, 046701-1–046701-9 (2004).

[49] C. P. Mellen, J. Frohlich, and W. Rodi, "Large-eddy simulation of the flow over periodic hills," in Proceedings of 16th IMACS World Congress, Switzerland, Lausanne, 2000, pp. 1–6.

[50] G. Almeida, D. Durao, and M. Heitor, "Wake flows behind two dimensional model hills," Exp. Therm. Fluid Sci. **7**, 87–101 (1993).

[51] C. Rapp and M. Manhart, "Experimental investigations on the turbulent flow over a periodic hill geometry," in 5th International Symposium Turbulence and Shear Flow Phenomena, Garching, Germany, 2001, Vol. 2, pp. 649–654.

[52] C. Rapp, F. Pfleger, and M. Manhart, "New experimental results for a LES benchmark case," in *Direct and Large-Eddy Simulation*, ERCOFTAC Series Vol. 13, edited by V. Armenio, B. Geurts, and J. Fröhlich (Springer Netherlands, 2010), pp. 69–74.

[53] C. Rapp and M. Manhart, "Flow over periodic hills—An experimental study," Exp. Fluids **51**, 247–269 (2011).

[54] See http://qnet-ercoftac.cfms.org.uk/w/index.php/UFR_3-30_Test_Case for Ercoftac; accessed 5 August 2017.

[55] L. Temmerman and M. A. Leschziner, "Large eddy simulation of separated flow in a streamwise periodic channel constriction," in Proceedings of 2nd International Symposium of Turbulence and Shear Flow Phenomena, KTH, Stockholm, 2001, pp. 399–404.

[56] L. Temmerman, M. A. Leschziner, C. P. Mellen, and J. Frohlich, "Investigation of wall-function approximations and subgrid-scale models in large eddy simulation of separated flow in a channel with streamwise periodic constrictions," Int. J. Heat Fluid Flow **24**, 157–180 (2003).

[57] S. Jakirlic, R. J. Zürker, and C. Tropea, Report on 9th ERCOFTAC/IAHR/COST workshop on refined turbulence modelling, ERCOFTAC Bulletin, Darmstadt University of Technology, 2001, pp. 36–43.

[58] S. Jakirlic, S. Saric, G. Kadavelil, E. Sirbubalo, B. Basara, B. Chaouat, "SGS modelling in LES of wall-bounded flows using transport RANS models: From a zonal to a seamless hybrid LES/RANS method," in Proceeding of the 6th Symposium on Turbulent Shear Flow Phenomena, Seoul, South Korea, 2009, Vol. 3, pp. 1057–62.

[59] Y. J. Jang, M. A. Leschziner, K. Abe, and L. Temmerman, "Investigation of anisotropy-resolving turbulence models by reference to highly-resolved LES data for separated flow," Flow, Turbul. Combust. **69**, 161–203 (2002).

[60] J. Fröhlich, C. P. Mellen, W. Rodi, L. Temmerman, and M. A. Leschziner, "Highly resolved large-eddy simulation of separated flow in a channel with streamwise periodic constrictions," J. Fluid Mech. **526**, 19–66 (2005).

[61] M. Breuer, N. Peller, C. Rapp, and M. Manhart, "Flow over periodic hills—Numerical and experimental study in a wide range of Reynolds numbers," Comput. Fluids **38**, 433–457 (2009).

[62] P. Balakumar, G. I. Park, and B. Pierce, "DNS LES and wall-modeled LES of separating flow over periodic hills," in *Center for Turbulence Research Proceedings of the Summer Program* (Center for Turbulence Research, 2014), pp. 407–415.

[63] B. Chaouat and R. Schiestel, "Hybrid RANS/LES simulations of the turbulent flow over periodic hills at high Reynolds number using the PITM method," Comput. Fluids **84**, 279–300 (2013).

[64] B. Chaouat and R. Schiestel, "A new partially integrated transport model for subgrid-scale stresses and dissipation rate for turbulent developing flows," Phys. Fluids **17**, 065106 (2005).

[65] See http://www.openfoam.com for Openfoam, the open source cfd toolbox; accessed 5 August 2017.

[66] B. P. Leonard, "The ultimate conservative difference scheme applied to unsteady one-dimensional advection," Comput. Methods Appl. Mech. Eng. **88**, 17–74 (1991).

[67] R. I. Issa, "Solution of the implicitly discretised fluid flow equations by operator-splitting," J. Comput. Phys. **62**(1), 40–65 (1986).

[68] A. Aldama, "Leonard and cross-term approximations in the anisotropically filtered equations of motion," in *Large Eddy Simulation of Complex Engineering and Geophysical Flows*, edited by B. Galperin and S. A. Orszag (Cambridge University Press, New York, 1983), pp. 539–557.

[69] J. O'Brien, J. Urzay, M. Ihme, P. Moin, and A. Saghafian, "Subgrid-scale backscatter in reacting and inert supersonic hydrogen-air turbulent mixing layers," J. Fluid Mech. **743**, 554–584 (2014).

[70] S. Liu, C. Meneveau, and J. Katz, "On the properties of similarity subgrid-scale models as deduced from measurements in a turbulent jet," J. Fluid Mech. **275**, 83–119 (1994).

[71] A. Cook, "Determination of the constant coefficient in the scale similarity models of turbulence," Phys. Fluids **9**(5), 1485–1487 (1997).

[72] P. Moin, K. Squires, W. Cabot, and S. Lee, "A dynamic subgrid-scale model for compressible turbulence and scalar transport," Phys. Fluids A **28**(3), 2746–2757 (1991).

[73] Advanced Research Computing Center. 2012. Mount Moran: IBM System X cluster. Laramie, WY: University of Wyoming, http://n2t.net/ark:/85786/m4159c; accessed 28 April 2017.

[74] Computational and Information Systems Laboratory. 2012. Yellowstone: IBM iDataPlex System (Wyoming-NCAR Alliance). Boulder, CO: National Center for Atmospheric Research, http://n2t.net/ark:/85065/d7wd3xhc; accessed 28 April 2017.